Geophysical Journal International

Geophys. J. Int. (2020) **223,** 915–933
Advance Access publication 2020 July 25
GJI Geomagnetism, Rock Magnetism and Palaeomagnetism

doi: 10.1093/gji/ggaa355

Beyond the second-order magnetic anisotropy tensor: higher-order components due to oriented magnetite exsolutions in pyroxenes, and implications for palaeomagnetic and structural interpretations

Andrea R. Biedermann,[1,2,3] Mike Jackson,[1] Martin Chadima,[4,5] Ann M. Hirt[2] and Joshua M. Feinberg[1]

[1] *Institute for Rock Magnetism, Department of Earth and Environmental Sciences, University of Minnesota, Minneapolis, MN, USA.*
E-mail: andrea.regina.biedermann@gmail.com
[2] *Institute of Geophysics, ETH Zurich, Zurich, Switzerland*
[3] *Institute of Geological Sciences, University of Bern, Bern, Switzerland*
[4] *AGICO Inc., Brno, Czech Republic*
[5] *Institute of Geology of the Czech Academy of Sciences, Prague, Czech Republic*

Accepted 2020 July 23. Received 2020 July 17; in original form 2020 January 9

SUMMARY

Exsolved iron oxides in silicate minerals can be nearly ideal palaeomagnetic recorders, due to their single-domain-like behaviour and the protection from chemical alteration by their surrounding silicate host. Because their geometry is crystallographically controlled by the host silicate, these exsolutions possess a shape preferred orientation that is ultimately controlled by the mineral fabric of the silicates. This leads to potentially significant anisotropic acquisition of remanence, which necessitates correction to make accurate interpretations in palaeodirectional and palaeointensity studies. Here, we investigate the magnetic shape anisotropy carried by magnetite exsolutions in pyroxene single crystals, and in pyroxene-bearing rocks based on torque measurements and rotational hysteresis data. Image analysis is used to characterize the orientation distribution of oxides, from which the observed anisotropy can be modelled. Both the high-field torque signal and corresponding models contain components of higher order, which cannot be accurately described by second-order tensors usually used to describe magnetic fabrics. Conversely, low-field anisotropy data do not show this complexity and can be adequately described with second-order tensors. Hence, magnetic anisotropy of silicate-hosted exsolutions is field-dependent and this should be taken into account when interpreting isolated ferromagnetic fabrics, and in anisotropy corrections.

Key words: Magnetic properties; Magnetic fabrics and anisotropy; Palaeomagnetism; Fourier analysis; Image processing; Numerical modelling.

1 INTRODUCTION

Exsolved micrometre- and submicrometre scale iron oxide lamellae within silicates often form lath or platelet morphologies. They are well suited for palaeomagnetic and palaeointensity studies, because their magnetization may be more stable over geologic time than that of interstitial iron oxide grains. The reasons for their extraordinary magnetic stability are that (1) their size and shape commonly give rise to stable single domain or vortex state magnetic behaviour and (2) they are protected against chemical alteration by their host silicate (Xu *et al.* 1997; Cottrell & Tarduno 1999; Renne *et al.* 2002; Feinberg *et al.* 2005; Tarduno *et al.* 2006; Selkin *et al.* 2008). Magnetite laths and platelets exsolved within plagioclase and pyroxenes are particularly reliable remanence carriers, whereas inclusions in biotite and amphiboles tend to show multidomain behaviour due to their larger size, and are therefore more easily (re)magnetized (Wu *et al.* 1974). Stable remanence carried by magnetite lamellae in pyroxene or plagioclase has been described in many rock types, for example gabbro (Evans *et al.* 1968; Palmer & Carmichael 1973; Davis 1981; Scofield & Roggenthen 1986; Yu & Dunlop 2001; Renne *et al.* 2002), dolerite (Morgan & Smith 1981), diabase (Hargraves & Young 1969), granodiorite (Wu *et al.* 1974), pyroxenite (Palmer & Carmichael 1973; Bogue *et al.* 1995), norite, anorthosite and others (Murthy *et al.* 1971; Geissman *et al.* 1988; Xu *et al.* 1997; Selkin *et al.* 2000, 2008). Similar to exsolved inclusions of iron oxides in mafic minerals on Earth, olivine containing exsolved inclusions of metallic iron or iron–nickel particles have been described as faithful recorders of pre-accretionary remanence in chondritic meteorites. These metallic inclusions are protected against chemical alteration by the surrounding olivine, and occur in single domain and vortex magnetic states (Lappe *et al.* 2011; Einsle *et al.* 2016).

Silicate-hosted iron oxide exsolutions generally display large aspect ratios, and their orientation is crystallographically controlled by the host silicate. In this study, the term 'exsolution' is used to describe iron oxides whose orientation and shape are crystallographically controlled by the host silicate, and 'inclusion' can be both unoriented or oriented phases. The preferred orientation of exsolved inclusions has been observed by various mineralogical methods (Bown & Gay 1959; Putnis 1979; Fleet *et al.* 1980; Schlinger & Veblen 1989; Feinberg *et al.* 2004; Wenk *et al.* 2011), and is also reflected by low-field magnetic anisotropy in silicate crystals (Lagroix & Borradaile 2000). Clinopyroxenes often contain two sets of elongated, lath-shaped exsolutions, one subparallel to the crystallographic [001] direction called Z inclusions and a second subparallel to [100] called X inclusions (Bown & Gay 1959; Fleet *et al.* 1980; Doukhan *et al.* 1990; Feinberg *et al.* 2004). Blades and flattened rods of magnetite have been observed in orthopyroxene, lying in the (010) plane and elongated along [001] (Fleet *et al.* 1980). A number of results have been reported for plagioclase: Wu *et al.* (1974) describe magnetite (along with some ilmenite) inclusions oriented parallel to chemical zonation planes. Up to four sets of magnetite needle orientations within plagioclase were observed in ocean floor gabbros from the Mid Cayman Rise Spreading Center (Davis 1981), and up to five in gabbro-norites from the Burakov intrusion, Russia (Sobolev 1990). Xu *et al.* (1997) describe magnetite needles elongated parallel to the (010) plane of plagioclase in rocks from the Banded Series, Stillwater Complex. Feinberg *et al.* (2006b) reported four orientations of magnetite needles in plagioclase from the Bushveld Complex, which in turn were repeated by various forms of plagioclase twinning. Some of these inclusions were crystallographically intergrown with ilmenite. Anorthositic gneiss from the Adirondack mountains contains one set of oxide needles, elongated subparallel to [001] of plagioclase (Wenk *et al.* 2011). Putnis (1979) described two sets of micrometer-sized oriented platelets containing dendritic iron oxides in the Rhum Layered Intrusion, Inner Hebrides. In chondrules, metallic blebs are preferentially aligned along edge and screw dislocation pathways, indicating that they were formed by *in situ* reduction (Leroux *et al.* 2003). Einsle *et al.* (2016) characterized their shape and orientation, and found oblate ellipsoids arranged in sheets parallel to (001) of olivine, with a wide range of orientations of the maximum dimensions. Because these iron and iron–nickel exsolutions have strong intrinsic magnetization, their shape and shape-preferred orientation will cause magnetic anisotropy, similar to that observed in preferentially oriented magnetite in terrestrial rocks. The ultimate shape and crystallographic orientation of all such exsolutions is related to the direction of most rapid Fe-diffusion within their silicate-host as well as the orientation of close-packed oxygen layers and/or chains in the silicate host. Preferentially aligned magnetite possesses shape anisotropy (Grégoire *et al.* 1995), and the crystallographic control on the orientation and geometry of exsolutions can lead to magnetite shape anisotropy in silicate crystals containing exsolved magnetite needles and plates. Once a rock's or chondrite's silicate minerals are preferentially aligned, then so are its constituent exsolutions, which then contribute to the total magnetic fabric.

Magnetic anisotropy affects both the direction and intensity of a rock's magnetization, which can introduce uncertainties in palaeomagnetic interpretations: (1) the recorded magnetization tends to deviate away from the applied field direction and towards an 'easy' magnetization axis and (2) the magnetization intensity becomes directionally dependent (Hargraves 1959; Fuller 1960; Fuller 1963; Rogers *et al.* 1979; Aitken *et al.* 1981). Therefore, palaeomagnetists seek to correct for these anisotropy effects prior to interpreting their data, and have developed numerous correction methods, for example strain marker removal, inclination flattening models, the elongation-inclination method or corrections based on the sample's measured anisotropy (King 1955; Lowrie *et al.* 1986; Anson & Kodama 1987; Jackson *et al.* 1991; Stamatakos & Kodama 1991; Tauxe & Kent 2004; Tauxe *et al.* 2008; Kodama 2012). When using the latter method, it is essential to characterize and correct for the partial remanence anisotropy of the mineral that carries the stable part of the magnetic remanence, rather than for example anisotropy of susceptibility or bulk remanence anisotropy (Selkin *et al.* 2000; Bilardello & Kodama 2010; Biedermann *et al.* 2019a). A complete description of the anisotropy of the remanence carriers is a crucial prerequisite for reliable palaeomagnetic corrections.

Conventionally, magnetic anisotropy is described mathematically by a symmetric second-order tensor, whose eigenvalues and eigenvectors represent the principal susceptibilities and their directions (Nye 1957; Girdler 1961; Jelinek 1977). Occasionally, second-order tensors do not capture the full magnetic variability of a specimen. For example, measurements collected using a high-field torque magnetometer on specimens of Tasmanian dolerite by Stacey (1960) show 4θ components that were attributed to the alignment of cubic crystallographic axes of magnetite. Later studies by Syono (1965) and Martin-Hernandez *et al.* (2006) report torque signals dominated by 4θ components with additional 2θ and 6θ contributions on mm-sized octahedral magnetite crystals, measured in fields between 50 mT and 2 T. Similar torque measurements (in fields between 265 mT and 2 T) on hematite and pyrrhotite crystals revealed higher-order components in their basal-plane magnetocrystalline anisotropy (Flanders & Schuele 1964; Flanders & Remeika 1965; Martin-Hernandez *et al.* 2008; Martin-Hernandez & Guerrero-Suarez 2012). Another example of the inherent limitations of second-order tensors was given by Coe (1966), who investigated the anisotropy of isothermal remanence (AIRM) acquired in a field of 700 mT, and stated that due to non-linearity, a '*[. . .] less restrictive type of analysis than that offered by tensors will be needed if anisotropy in different materials is to be quantitatively compared using [the AIRM] method*'. Of particular importance for this study is that silicate-hosted magnetite exsolutions may themselves contain secondary sets of ulvöspinel or ilmenite lamellae, which along with their needle-shaped morphology give rise to directionally dependent strong-field AIRM behaviour that cannot be accurately described using second-order tensors (e.g. Feinberg *et al.* 2005, 2006a). It is an open question whether such higher-order complexities are attributed to specific minerals, or if they are field-related. Independent of their origin, other ways of representing anisotropy data include plotting the measurements taken in a plane (Flanders & Schuele 1964), or showing contour plots when directional data were not obtained in planes (Hrouda *et al.* 2018).

Given the importance of silicate-hosted exsolutions in recording information about the strength and direction of the ancient geomagnetic or extraterrestrial magnetic fields, and the palaeogeography of tectonic plates, a thorough understanding of their magnetic anisotropy is needed. Here, we focus on the magnetic anisotropy carried by exsolved inclusions in clinopyroxene and clinopyroxene-bearing rocks, particularly in high fields. Low-field measurements were conducted on a subset of samples to further investigate field-dependence. For both, the main goal of this study was to determine whether second-order tensors represent the anisotropy adequately.

Additionally, we present a model that calculates the magnetic torque in a plane based on the iron oxide particle size and orientation distribution as obtained from image analysis on backscattered electron images.

2 MATERIAL AND METHODS

2.1 Sample description

Two types of samples were used in this study (Table 1): (1) clinopyroxene single crystals and (2) clinopyroxene-bearing rocks. Single crystals include clinopyroxenes from Tenerife (Canary Islands, Spain), whose paramagnetic anisotropy was described in Biedermann *et al.* (2015), and clinopyroxene single crystals from the Messum Complex (Namibia) with oriented magnetite inclusions and stable remanence (Renne *et al.* 2002; Feinberg *et al.* 2004, 2005). Pyroxene-bearing rock samples include oxide gabbro and layered troctolite from the Nickel Lake Macrodike, Duluth Complex (MN; USA, Finnes 2012), gabbronorites from the Bushveld Complex (South Africa, Feinberg *et al.* 2006b) and ocean floor gabbro from the ODP 735B drill hole (Worm 2001; Feinberg *et al.* 2005). The mineralogy and magnetic properties of these samples (including magnetic anisotropy described by second-order tensors) have been described in the studies cited above, and their (partial) anhysteretic and isothermal remanence anisotropies (as second-order tensors) are reported in Biedermann *et al.* (2019a,b, 2020a,b).

The single crystals from Tenerife are a few mm to cm in size and were crystallographically oriented based on crystal habit and Laue diffraction prior to magnetic measurements. Pyroxene crystals from the Messum Complex were smaller, on the order of 1 mm, and cemented into hollow quartz tubes. Rock samples were 2.5 cm cores with a length of 2.2 cm or shorter. Sample coordinate systems for the rocks (*z* along the cylinder axis) were chosen arbitrarily, and are unrelated to geographic or tectonic reference frames. After completion of magnetic measurements, oriented polished thin sections in the *xy* plane were prepared from a subset of the cores used for magnetic analyses. Optical microscopy as well as backscattered electron (BSE) images, obtained on a JEOL JXA-8900 Electron Probe Microanalyzer at the University of Minnesota, show that several sets of exsolutions lamellae are present in these rock samples, confirming the findings of previous studies (Fig. 1). Chemical analyses revealed that the lamellae were mostly magnetite, with a small number being composed of ilmenite. Note that analysing the composition of these small exsolutions is challenging, because the interaction volume of a focused electron beam often exceeds the thickness of the iron oxide exsolutions. This characteristic of the particles of interest prevents a full quantitative determination of oxide compositions, unless more involved transmission electron microscopy methods are used. Nevertheless, we observe that in some crystals, the Fe/Ti ratios of the oxides correlate with particular exsolution orientations (unpublished data).

2.2 Torque magnetometry

Magnetic torque was measured on a home-built torque magnetometer at the Laboratory of Natural Magnetism (LNM), ETH Zurich (Bergmüller *et al.* 1994). Measurements were collected over three perpendicular planes, while rotating the sample in 10° increments, using six fields between 0.5 and 1 T for strongly magnetic samples, or eleven fields between 0.5 and 1.5 T in weaker samples, where 1.5 T is the upper instrumental limit. Standard torque curves

Table 1. Overview of samples and locations, magnetic mineralogy and averages of previously reported susceptibilities and low-field anisotropy parameters.

	Name prefix	# specimens	Location	Rock type	Magnetic mineralogy	Average low-field mean susceptibility ($m^3 kg^{-1}$)	Average low-field mean deviatoric susceptibility ($m^3 kg^{-1}$)	Average low-field anisotropy *P* value	References
Single crystals									
	T	6	Tenerife	Pyroxene crystal	(Ti-) Magnetite	$(1.5 \pm 0.6)\times10^{-5}$	$(1.6 \pm 1.2)\times10{-}6$	1.3 ± 0.2	Biedermann *et al.* (2015)
	M	9, too weak to analyze	Messum Complex, Namibia	Pyroxene crystal	Ti-magnetite, exsolved to magnetite and ulvöspinel	not specified	not specified	not specified	Renne *et al.* 2002; Feinberg *et al.* (2004, 2005)
Rocks									
	NLMD_NxG	2	Duluth Complex, MN, USA	Oxide gabbro	PSD magnetite and Ti-magnetite; sulphides in some samples	$(6.2 \pm 1.8)\times10^{-6}$	$(3.0 \pm 1.7)\times10^{-7}$	1.11 ± 0.04	Finnes (2012), Biedermann *et al.* (2019a,b, 2020a,b)
	NLMD_NTl	3	Duluth Complex, MN, USA	Layered troctolite	PSD magnetite and Ti-magnetite; sulphides in some samples	$(7.2 \pm 1.3)\times10^{-6}$	$(2.7 \pm 0.9)\times10^{-7}$	1.09 ± 0.01	Finnes (2012), Biedermann *et al.* (2019a,b, 2020a,b)
	BG	4	Bushveld Complex, South Africa	Gabbronorite	Ti-magnetite, ilmenite needles, hematite platelets	$(1.9 \pm 0.4)\times10^{-6}$	$(7.7 \pm 4.0)\times10^{-8}$	1.10 ± 0.05	Feinberg *et al.* (2006b), Biedermann *et al.* (2019a,b, 2020a,b)
	ODP735	4	ODP hole 735B	Ocean floor gabbro	Primary ilmenite and Ti-magnetite, secondary magnetite, some sulphides	$(2.5 \pm 2.9)\times10^{-6}$	$(1.2 \pm 1.3)\times10^{-7}$	1.12 ± 0.03	Worm (2001), Feinberg *et al.* (2005), Biedermann *et al.* (2019a,b, 2020a,b)

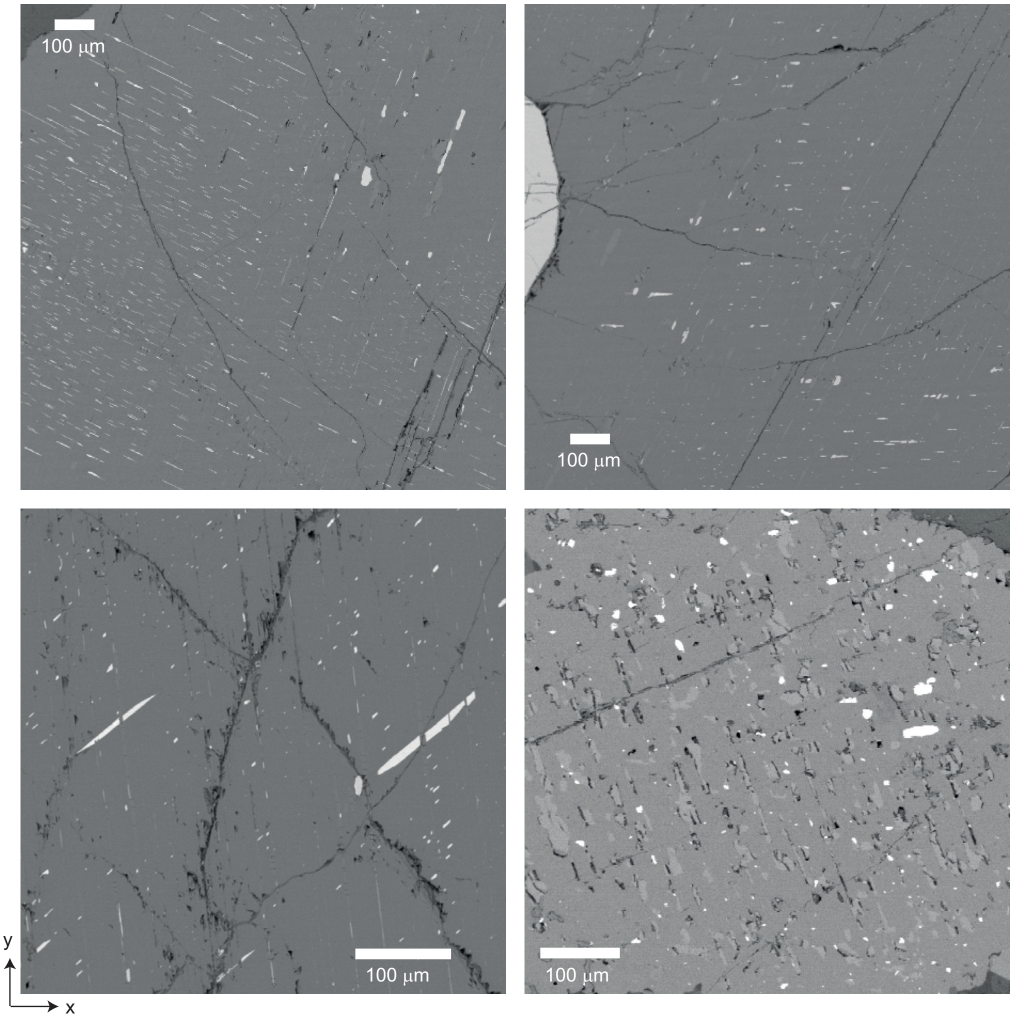

Figure 1. BSE images showing oriented oxide exsolutions lamellae in pyroxene grains of NLMD_NxG_01010401, Duluth (top panels), NLMD_NTl_01010201, Duluth (bottom left), and BG1.23a, Bushveld (bottom right). Lamellae occur in a range of sizes and aspect ratios, and in distinct sets of orientations. Larger, potentially occluded, oxide grains are also observed. Intermediate gray lamellae in the backscatter images are exsolved orthopyroxene and amphibole within the host clinopyroxene.

were obtained while the sample was rotated from 0° to 10°, 20°, . . . 360°, and rotational hysteresis (measured on a subset of samples, mainly single crystals) while the sample was rotated from 360°, 350°, . . . 0°, 0°, 10°, . . . 360°. Rotational hysteresis was measured in eleven fields between 0.5 and 1.5 T on single crystals, and six fields between 0.5 and 1.0 T on the rock sample. Fourier analysis was applied to these measurements to define the contributions to anisotropy from 2θ components that define the second-order tensor, as well as the remanent magnetization (1θ), and higher-order components.

2.3 Low-field susceptibility

Low-field magnetic susceptibility was measured on four single crystals from Tenerife, using an AGICO MFK1 susceptibility bridge in a field of 200 A m^{-1} and a frequency 976 Hz. Initially, directional susceptibility was measured in 10° increments in three perpendicular planes, that is using the same set of directions as for torque magnetometry, at the LNM. Because these measurements were noisy, a second set of measurements was obtained on the MFK2 at AGICO, using AGICO's one-axis rotator and an adapted version of the instrument-control software, measuring susceptibility at 5.625° intervals during eight rotations of the sample in each of the three planes. This procedure was repeated five times, yielding a total of 40 data sets of susceptibility as a function of rotation. Note that these measurements are reported in units of instrument response, and are not calibrated nor normalized to susceptibility units. The MFK2 uses the same default measurement field and frequency as the MFK1, but is equipped with improved electronics that increase signal quality.

2.4 Oxide imaging and particle analysis

Oxides were imaged in selected rock samples using backscattered electrons on the JEOL JXA-8900 Electron Probe Microanalyzer at the Department of Earth Sciences, University of Minnesota. Comboscans enabled the sequential mapping of large areas of the sample surface (2.5 cm diameter), while maintaining sufficiently high resolution to identify submicrometre inclusions. The chemical composition of oxides was determined by point analyses as well as chemical mapping in selected areas, using wavelength-dispersive X-ray spectroscopy.

For the purpose of this study, we were mainly interested in the size, shape and preferred orientation of the oxide exsolutions. BSE images were analysed using the Fiji version of the freely available ImageJ software (Schindelin *et al.* 2012; Schneider *et al.* 2012). After thresholding the BSE images to isolate the oxide particles, particles were defined, and best-fit ellipses computed for each particle. The length and orientation of the major and minor axes of each best-fit ellipse were then used for magnetic modelling.

2.5 Modelling magnetic anisotropy and torque

Due to its strong magnetization, the magnetic anisotropy of magnetite is controlled by particle shape, or more specifically, by the demagnetization tensor that is related to particle shape. Although magnetocrystalline anisotropy is measurable in for example octahedral magnetite crystals (Syono 1965; Martin-Hernandez *et al.* 2006), this contribution to anisotropy is often masked by the stronger shape anisotropy in non-equidimensional magnetite grains (Borradaile & Henry 1997; Grégoire *et al.* 1998; Borradaile & Jackson 2010). Stacey (1960) found both a dominant 2θ component related to slightly elongated magnetite (up to 50 per cent elongation) and a 4θ component due to magnetocrystalline anisotropy in a set of dolerite samples. Due to the large aspect ratios of the magnetite grain dimensions in this study, their anisotropy is modelled by shape anisotropy only. Demagnetization tensors are readily defined for ellipsoidal bodies, but not for irregular shapes (Osborn 1945). Therefore, the magnetic anisotropy was approximated using the best-fit ellipses obtained from image analysis.

Image analysis provides particle shapes and sizes in 2-D, but demagnetization tensors need to be defined in 3-D. Therefore, the magnetic anisotropy models assume that the major axis of the best-fit ellipse is the symmetry axis of a prolate 3-D ellipsoid. Hence, the models presented here are best suited to represent the anisotropy of needle-shaped magnetite exsolutions.

Magnetic torque has been modelled in two different ways: (1) assuming that the magnetization is fully saturated and parallel to the applied field, in which case torque is controlled by differences in demagnetization energy in different directions, and independent of field (Martín-Hernández & Hirt 2001) and (2) assuming that magnetization intensity reached saturation, but the magnetization vector still deviates from the field direction and towards the easy axis of the particle (Abbott *et al.* 2007). Note that the second model contains two parts; in low fields, the magnetization direction is constant and defined by the field orientation and body dimensions, and the magnetization intensity increases linearly with field until it reaches saturation; as the field increases above this intensity saturation field, the magnetization intensity remains constant, but its direction rotates towards the applied field direction. These directional changes result in field-dependent torque curves even above the field that saturates magnetization intensity. Because the deviation of the magnetization from the field direction in a given field is controlled by shape anisotropy, the effect will be stronger for strongly anisotropic particles, both for magnetization directions and field-dependence of torque. It is this part of the model, that is above intensity saturation, but magnetization direction still deviating from field direction, that is relevant for the fields used in the present study. At sufficiently large fields, the deviation between magnetization and field directions approaches zero, and the differences between the models become smaller until they coincide when full saturation (in intensity and direction) is reached. The threshold for fields to be sufficiently large depends on the particle shape, and stronger fields are needed for particles with higher ratio of longest to shortest axes. Magnetic anisotropy and torque were calculated for each particle separately, and these contributions were added (1) with equal weight for each particle or (2) scaled by the particle area measured from image analysis, to obtain the overall anisotropy of the rock. Because BSE images and particle analysis are available for the *xy*-plane, models were computed for this plane, and compared to measurements in the same plane.

3 RESULTS

3.1 Torque magnetometry

Selected torque curves for pyroxene single crystals and the rock samples are shown in Fig. 2. For dia/paramagnetic samples one would expect 2θ signals symmetric around 0, with torque increasing linearly with applied field squared. Fully saturated ferrimagnetic phases with uniaxial shape anisotropy display a 2θ signal, symmetric around 0, and independent of applied field (Martín-Hernández & Hirt 2001). In this study, we use the term ‘symmetric’ torque curve to describe a signal that can be represented by pure sine/cosine waves, with mirror symmetry across their maxima and minima, and inversion symmetry through their zero crossings. In other words, positive and negative peaks are equal in intensity and shape, and their ascending and descending branches have the same slopes. Conversely, the torque signal observed for samples investigated here can be asymmetric and/or skewed, and can contain higher-order components. Asymmetric torque curves have different intensities for positive and negative peaks, and in skewed curves, the increasing and decreasing branches of each peak have different slopes. For some samples and measurement planes, the shape of the torque curves is field-dependent.

Fourier component analysis reveals that the contribution of the 2θ component covers a range from 20 to 98 per cent, along with <1 to 72 per cent 4θ, and <1 to 16 per cent 6θ components (Fig. 3). Residual portions of the signal are mainly 1θ components related to unsaturated remanence. Note that the relative contributions of each component are generally different for each measurement plane, and also vary with field.

Clinopyroxene single crystals from Tenerife display the highest 4θ contribution in the [100]–[001] plane, up to 32 per cent, while it is up to 19 per cent in the (100)–[010] and [010]–[001] planes. For all three planes, the higher the measurement field, the more prominent the 2θ component, while the 4θ component becomes less important. The amplitude of the torque signal, approximated by half the peak-to-peak-distance, and the magnitude of the 2θ component increase non-linearly with field, whereas the magnitude of the 4θ component shows a non-linear decrease with field. Because of their small sample size, the torque signal of the Messum crystals is noisy, resulting in artificially strong higher-order components and will not be interpreted further.

The torque signals of the rocks can also have different relative contributions in separate measurement planes. The relative contribution of the 2θ component can increase or decrease with higher fields. Some samples show a more prominent 2θ component in higher fields in some planes, but less prominent 2θ component in others. Peak-to-peak distances and 2θ as well as 4θ component magnitudes increase with field for most samples.

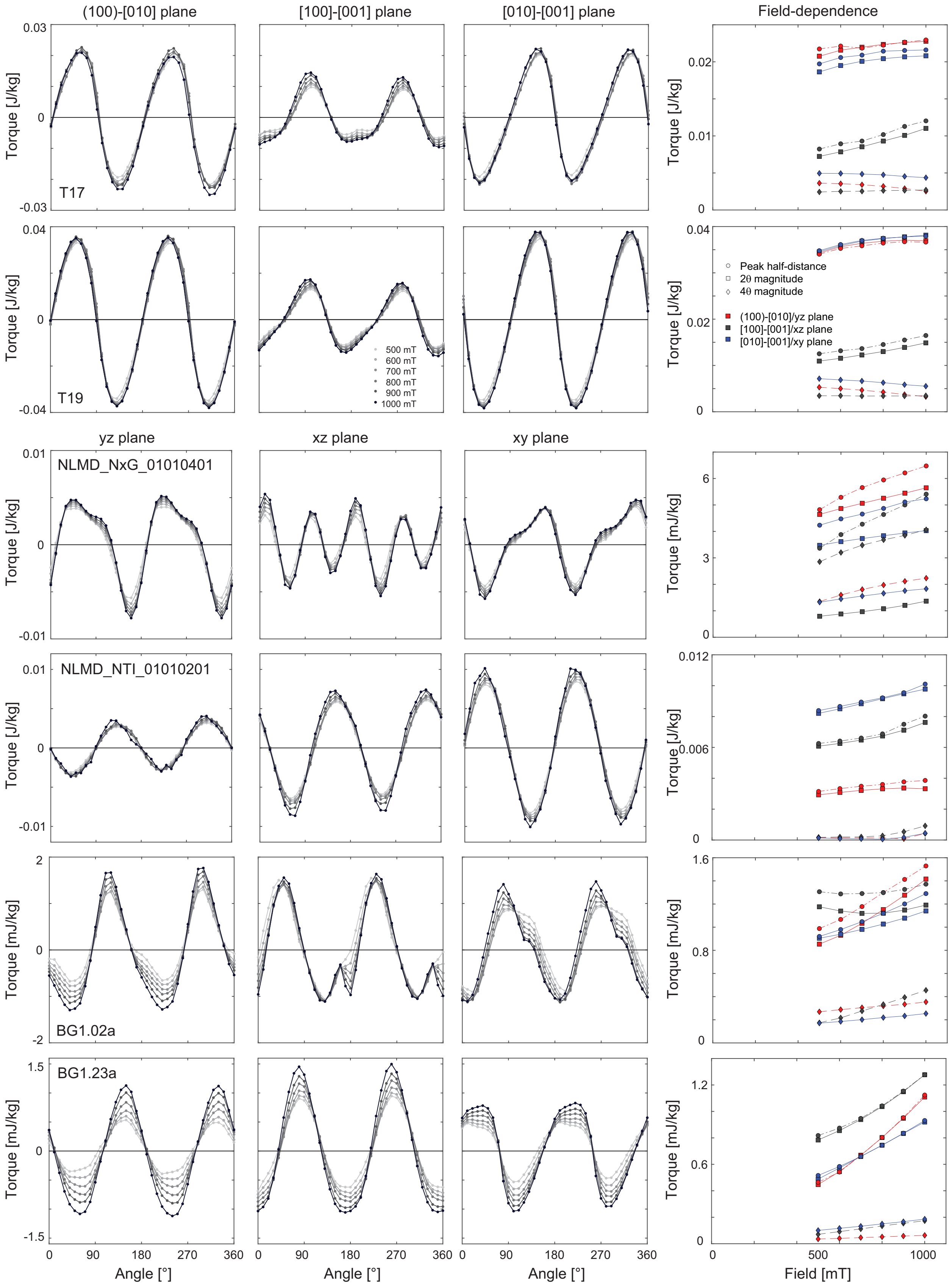

Figure 2. Examples of torque signals observed in single crystals and rock samples. Note that most torque curves contain higher-order components, and/or are asymmetric or skewed. This complexity is reflected in the complicated field-dependence of the torque signal, given here as half of the peak-to-peak distance, and the magnitude of the 2θ and 4θ components, respectively.

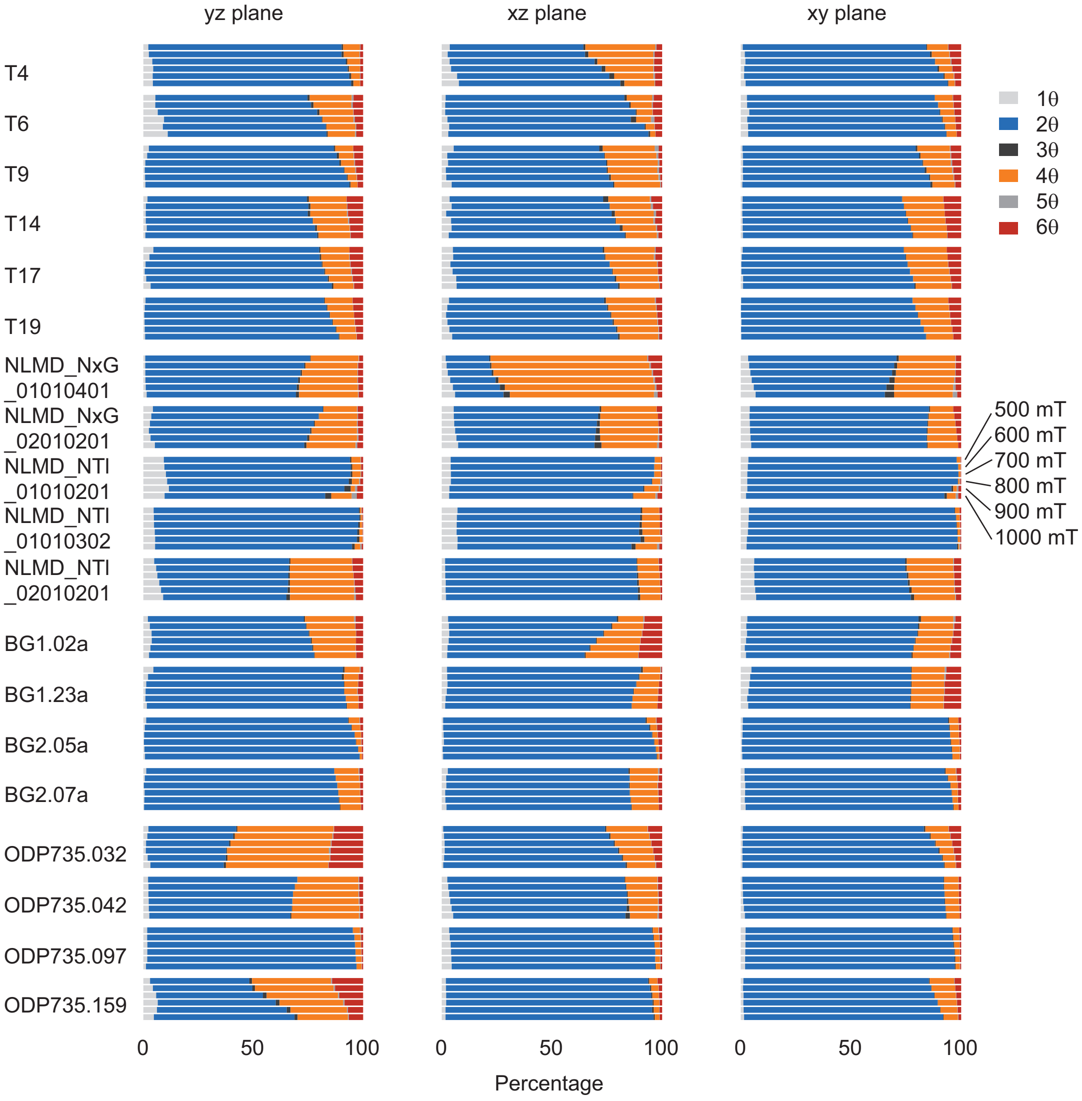

Figure 3. Fourier component analysis of the torque signal. The relative contributions of 1θ to 6θ components are shown in 18 data sets per sample, corresponding to six fields measured in each plane.

Rotational hysteresis measurements were conducted on three single crystals, T4, T6 and T17, and one rock sample, NLMD_NxG_01010401. Single crystals were measured in 11 fields between 0.5 and 1.5 T. The rock sample was too strongly magnetic to be measured in high fields, so that it was measured in six fields between 0.5 and 1.0 T. All single crystals show rotational hysteresis in each measurement plane, and every field (Fig. 4). Rock sample NLMD_NxG_01010401 does show rotational hysteresis, but it is a smaller proportion of the sample's torque signal than the rotational hysteresis displayed by the single crystals.

3.2 Low-field susceptibility anisotropy

Low-field susceptibility anisotropy is characterized predominantly by 2θ signals (Fig. 5). Averaged over all 40 data sets (i.e. five repeat measurements with eight sample rotations each), the contribution of the 2θ component is >95 per cent in all samples and all measurement planes. In the [010]–[001] plane of T4, it contributes even >99 per cent to the total signal. For the individual rotations, the 2θ contributions are slightly lower, 87.4–99.0 per cent, likely due to the larger noise level in the individual measurements compared to the average. Of particular interest for this study is that the 4θ components observed in high fields, as shown in Figs 2–4, are largely absent from the low-field data (<3 per cent in the averaged data sets).

3.3 Image analysis and models

All rock samples contain large irregular oxide grains, as well as highly elongated exsolution lamellae within the pyroxenes. Because image analysis is a 2-D technique, it provides information on the particle shape in 2-D, but does not distinguish between, for example needles and platelets that are viewed in cross-section. For the same reason, aspect ratios obtained from image analysis provide a lower threshold for the real particle anisotropy. Nevertheless, these 2-D particle properties can be used to estimate their orientation distribution to a first-order approximation. The estimated orientation and size of each particle was used to model the magnetic anisotropy, under the assumption that all oxide particles are magnetite.

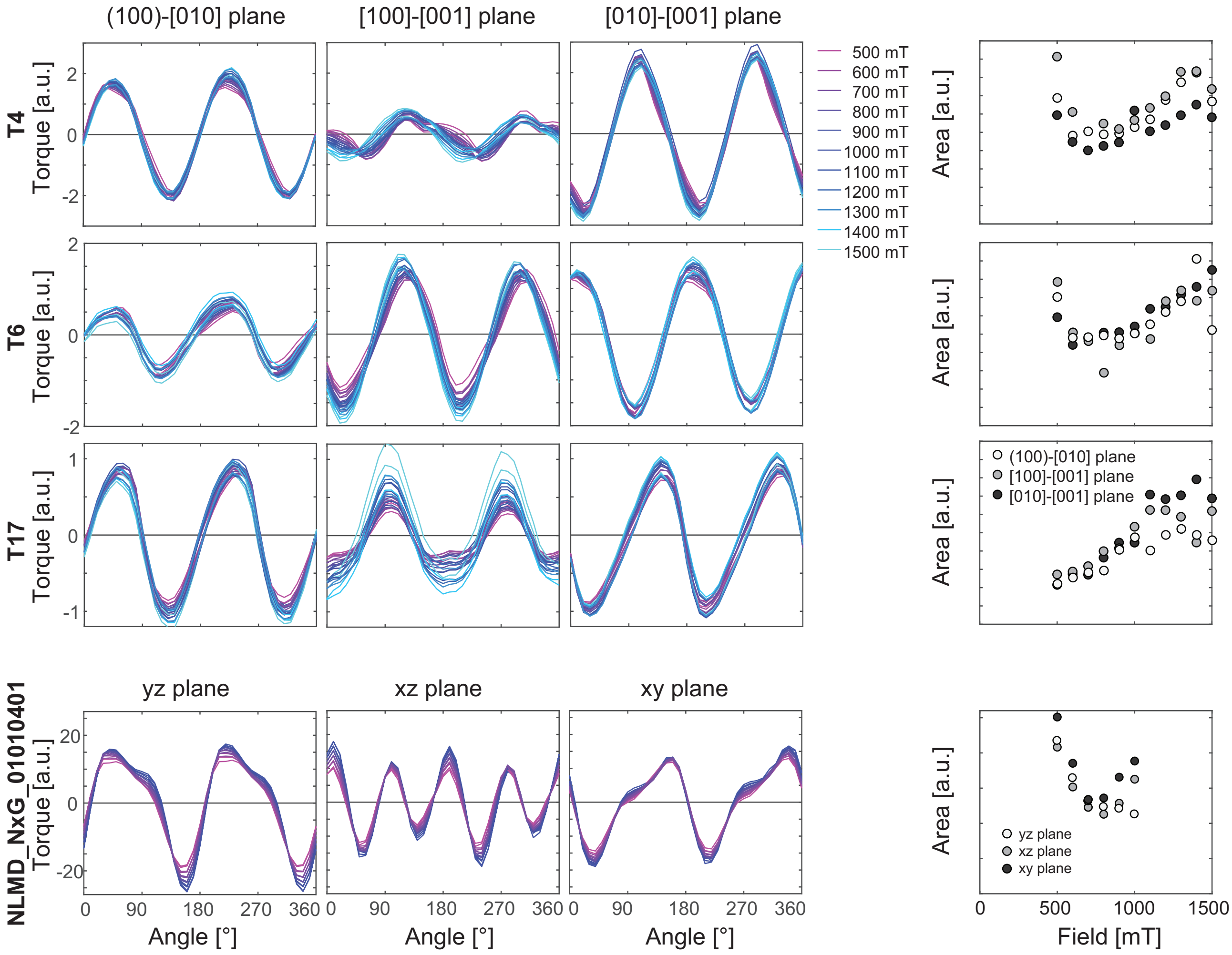

Figure 4. Rotational hysteresis for three single crystals, measured in fields between 0.5 and 1.5 T, and one rock sample, measured between 0.5 and 1 T. Torque and area enclosed by the upper and lower branch of the hysteresis loop are given in arbitrary units (a.u.).

An overview of how the geometric properties of particles are obtained from the original BSE image is given in Fig. 6. Note that particles defined by only a few pixels in area will always have orientations of 0°, 90°, 180° or 45° and 135°, which introduces artefacts in the orientation density, related to the orientation of the pixels and coordinate system. These particles were removed prior to further analysis. Fig. 6 displays orientation densities for all particles (note the artefact at 135°) as well as particles larger than four pixels (no obvious artefact).

Some of the rock samples show several distinct maxima of oxide orientations (NLMD_NxG_01010401, NLMD_NTl_01010201 and ODP735.032) whereas others (BG1.23a and BG2.05a) show rather uniform distributions, and ODP735.097 displays one broad maximum (Fig. 7). Another interesting point is the correlation between aspect ratio and particle size. Sample NLMD_NxG_01010401 has a unique character in that particle aspect ratios increase up to a certain size. After this threshold size, aspect ratios are small. Sample NLMD_NxG_01010401 possesses the most elongate particles (aspect ratios up to 150) of all rock samples investigated here. All other samples show a more gradual variation of aspect ratios with particle size.

Based on the results from image analysis, expected torque curves in the *xy*-plane were calculated. Fig. 8 illustrates the different models for an example with only two particles. These particles were chosen arbitrarily, and torque curves were modelled for six fields between 0.5 and 1 T. Some characteristics of each model can already be observed from this simple two-particle model: (1) The torque curves of each particle, as well as the superposed torque signal as calculated from the MH01 model are pure 2θ signals, symmetric around 0, and field-independent, with the magnetization strictly parallel to the applied field. (2) In the A07 model, the magnetization is oriented in the direction that minimizes the sum of the external field (Zeeman) energy and the shape anisotropy energy (Fig. 8). As a result, the individual torque curves calculated from this model are skewed. This skewness results in higher-order Fourier components of each individual torque curve. The combined torque curve is skewed, contains higher-order Fourier components, and is not symmetric around zero. The shape of the torque curve as well as the contributions of each Fourier component are field-dependent. (3) The different weighting schemes result in peaks being at different angles in the MH01 model, but lead to different shapes and hence different Fourier components for the A07 model. It is interesting to

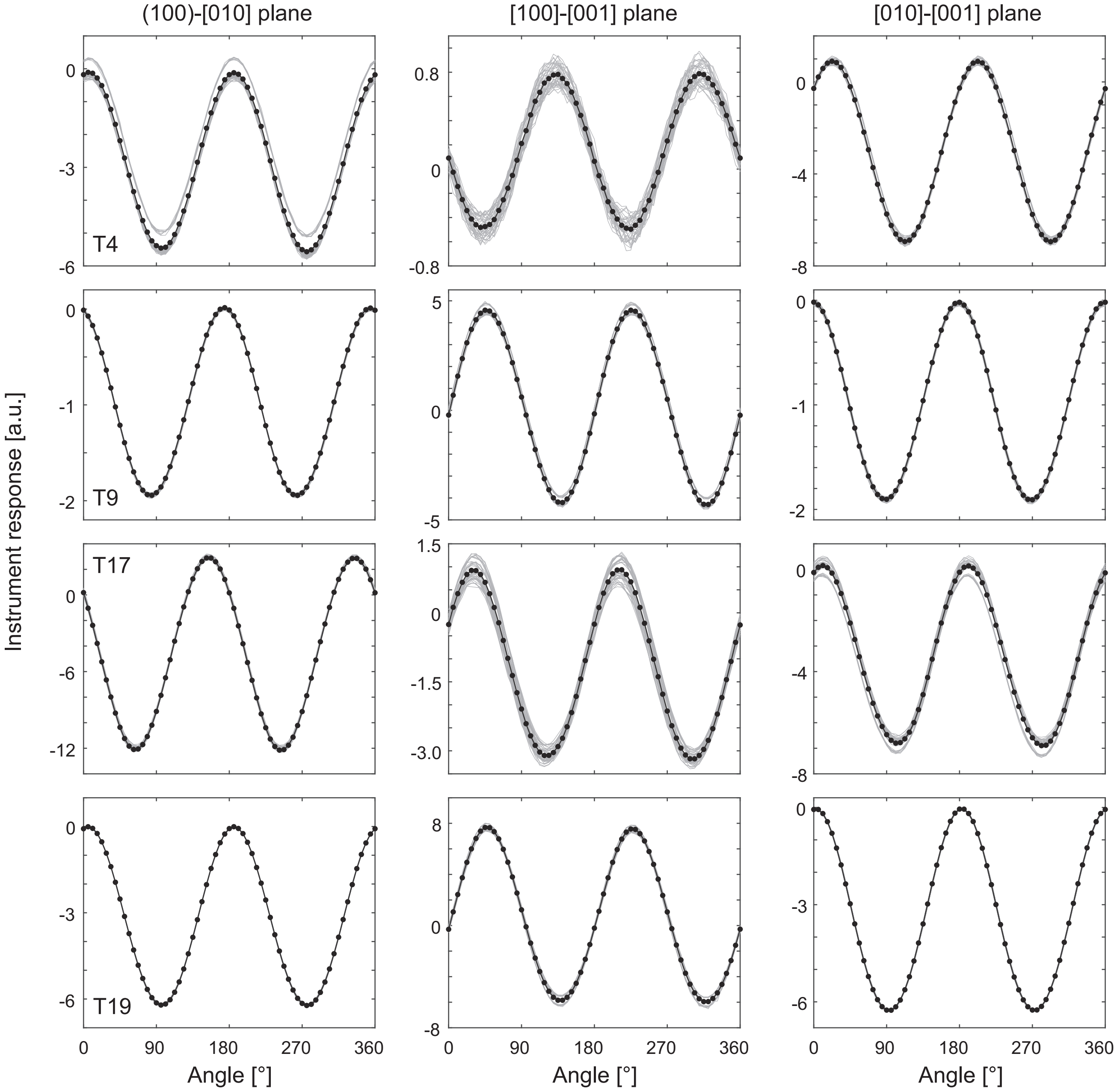

Figure 5. Low-field susceptibility in three perpendicular planes is dominated by 2θ signals. Figure shows individual rotations (grey) and average of 40 sample rotations (black) for four Tenerife single crystals in each crystallographic plane.

note that the A07 torque calculations, based on two arbitrary particles from an arbitrary grain in sample NLMD_NxG_01010401 and weighted by particle area, generate torque curves that qualitatively resemble those measured.

More advanced models include all particles that were measured for each rock sample. These models, and the corresponding measurements are shown in Fig. 9. They were computed for fields between 0.5 and 1 T, and illustrate the same differences between the MH01 and A07 sets of torque predictions as noted for the two-particle model. The models do not always fully reflect the measured data, which may be explained by the models considering only magnetite shape anisotropy while measurements include other anisotropy contributions, imperfect image resolution as well as the fact that only one 2-D image of particles was analysed rather than a full volume in 3-D. However, A07 predictions do reproduce some of the key features of the measurements, namely (1) torque curves that contain higher-order components in addition to the 2 θ signals expected from a second-order tensor, (2) skewed torque curves and (3) torque signals not symmetric around 0. It is interesting to note that for some samples (e.g. NLMD_NxG_01010401, BG2.05a, ODP735.032 and ODP735.097) the model that gives equal weight to each particle yields a closer reproduction of the measured torque data, while for BG1.23a it is the weighted average that matches better. The shape of the measured torque signal for samples NLMD_NxG_01010401 and BG1.23a is better reproduced by the models using the threshold field at which magnetization intensity is just saturated than by the models for fields of 0.5–1 T. This may indicate that our models underestimate the shape anisotropy

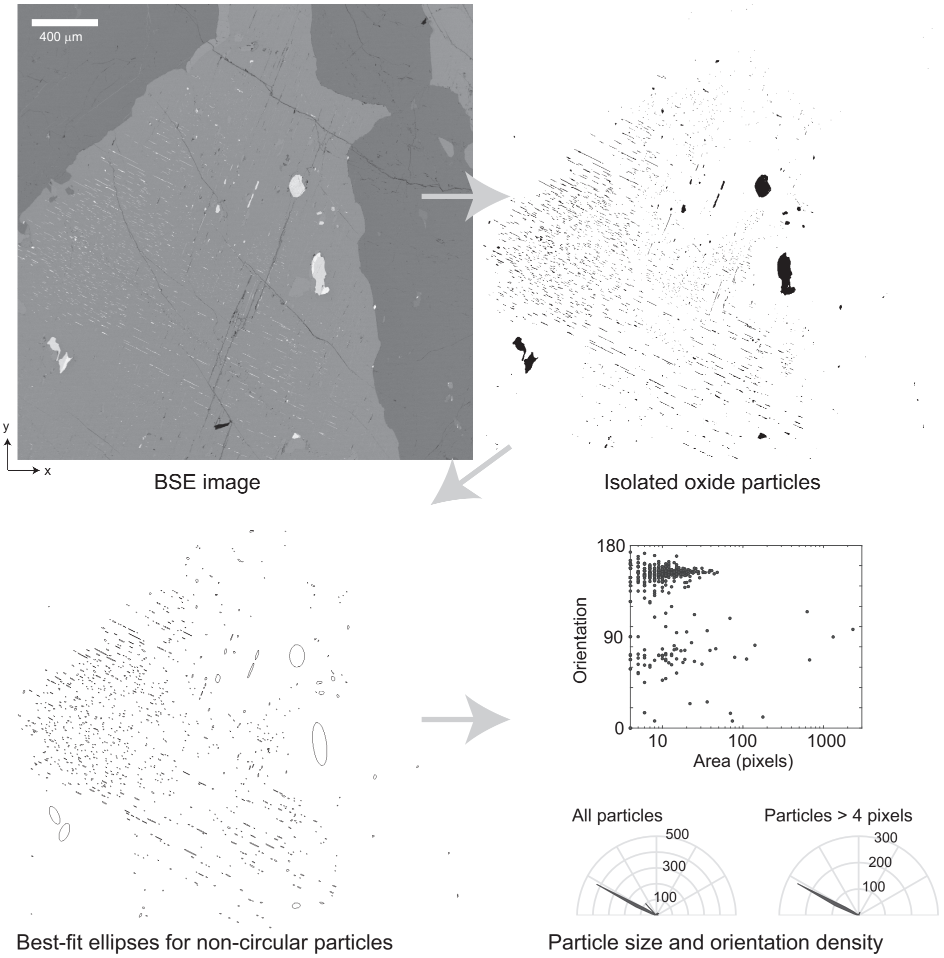

Figure 6. Example of the process from BSE image to isolated oxides, best-fit ellipses, and particle size and orientation density distributions. The BSE image shown here pictures part of a clinopyroxene grain in sample NLMD_NxG_01010401, with many small exsolved grains of similar orientation, and some larger grains of a different orientation. Numbers in the polar histograms indicate the number of particles of a certain orientation, using 5° bins. Resolution 0.4 pixels per micrometer.

of the particles, or that small particles that were not resolved in the BSE image are contributing to the magnetic measurements. Note that the threshold field at which the magnetization intensity saturates depends on the particles' size and shape distributions, and the direction of the applied field. Due to their range of aspect ratios, different particles in a single sample will reach intensity saturation at different field values. The field taken as threshold here is the maximum field at which any iron oxide exsolution in the sample reaches intensity saturation in all field directions, and this field corresponds to *ca*. 300 mT. Above this intensity saturation field, the magnetizations in the A07 model rotate towards the field direction, until full saturation, in which case both the A07 and MH01 models would provide the same results.

3.4 Predicting anisotropy for clinopyroxene-hosted exsolutions with different aspect ratios

The same models have been used to calculate the high-field magnetic torque for the exsolutions lamellae hosted within clinopyroxene single crystals. For these predictions, we assumed X inclusions elongated at 104° to [001], and Z inclusions at 9° to [001] of the clinopyroxene, and in the [100]–[001] plane. A first model was calculated with particle sizes of 20∗1∗1 μm for X inclusions, and 60∗1∗1 μm for Z inclusions, simplified from maximum dimensions reported by Fleet *et al.* (1980), in different proportions (Fig. 10). The MH01 torque models always predict pure 2θ signals independent of field, with maximum torque at different angles depending on the proportion of X and Z inclusions. These models show highest anisotropy when either the X or the Z inclusions dominate, but low anisotropy when both contributions are similar. Models based on Abbott *et al.* (2007)'s equations predict different shapes of torque curves for different proportions of X and Z inclusions. There are peaks related to both X and Z inclusions when both are present, introducing higher-order Fourier components. Additionally, the shapes of the modelled torque curves as well as the Fourier components are field-dependent, with stronger contributions from higher-order components at lower fields. This is reflected in the nonlinear decrease of the 4θ magnitude with increasing field, and nonlinear increase of the 2θ magnitude with field, similar to the measurements on pyroxene single crystals from Tenerife (*cf*. Fig. 2). Depending on the model composition and field, the contribution of 4θ components varies between *ca*. 10 and *ca*. 70 per cent of the torque signal. The observed contributions of 20–30 per cent in the single crystals from Tenerife fall within this range.

Additional models show the effect of different aspect ratios of the X and Z inclusions for various amounts of each orientation (Fig. 11).

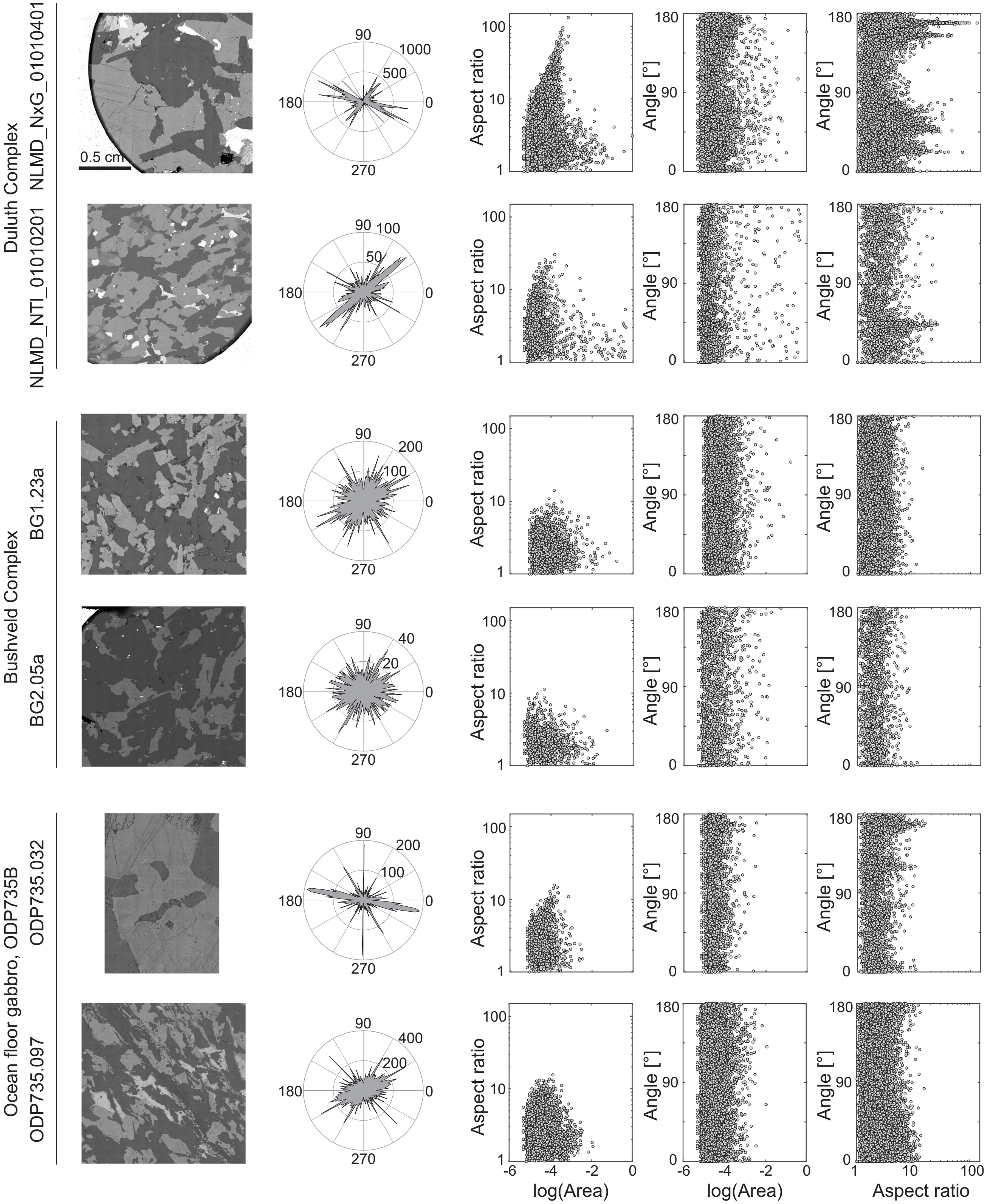

Figure 7. Image analysis results for rock samples, showing orientation density functions and correlations between particle size, aspect ratio and orientation for all non-circular particles. Number of particles analysed are 20 397 for NLMD_NxG_01010401, 3838 for NLMD_NTl_01010201, 9356 for BG1.23a, 1740 for BG2.05a, 5300 for ODP735.032, and 12 726 for ODP735.097. Note that maxima at 0°, 45°, 90°, ... are likely artefacts that have not been removed. Resolution 0.7–1 pixel per micrometer. Area given in mm^2, so that log(Area) = –6 indicates a grains of 1 μm × 1 μm, and log(Area) = 0 corresponds to 1mm × 1 mm.

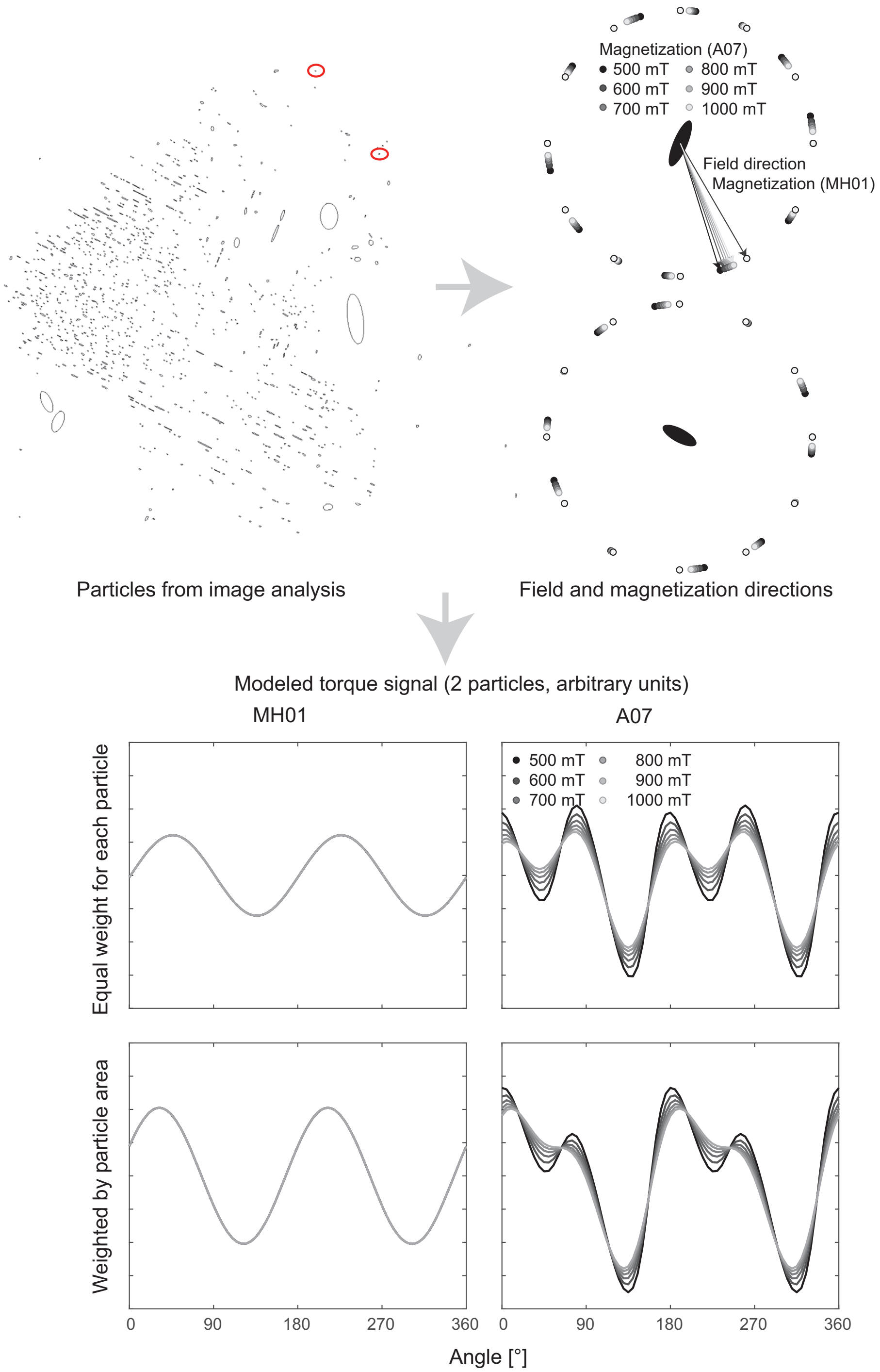

Figure 8. Magnetization and torque modelled for two particles from the grain shown in Fig. 6. Magnetization and torque of each particle were computed in two ways, (1) based on the model given by Martín-Hernández & Hirt (2001) (MH01) and (2) based on the model given in Abbott *et al.* (2007) (A07). The difference between these two models is whether the magnetization is parallel to the field, or deviated away from the field direction by shape anisotropy. The combined torque of both particles is calculated by (1) assuming each particle contributes equally or (2) weighting the contributions of particles by their respective areas.

These models assign equal weight to each particle, so that the results are independent of particle size. The smaller the aspect ratio, that is the less elongated the particles, the weaker the shape anisotropy, so that the magnetization direction is closer to that of the applied field, resulting in a stronger contribution of the 2θ component. In the limiting case of an aspect ratio equal to 1, the magnetocrystalline anisotropy of magnetite is expected to be observed; however, the models presented here only predict the anisotropy due to particle shape. When one orientation of exsolutions dominates the torque signal, then the 2θ component contributes more to the total torque, whereas higher-order components are more prominent when the anisotropy contributions of X and Z inclusions are comparable. The relative contributions of Fourier components vary with aspect ratios up to around 10, and remain stable for aspect ratios larger than 20. Note that, even if the Fourier component proportions are nearly constant for aspect ratios >20, the amplitude of the torque

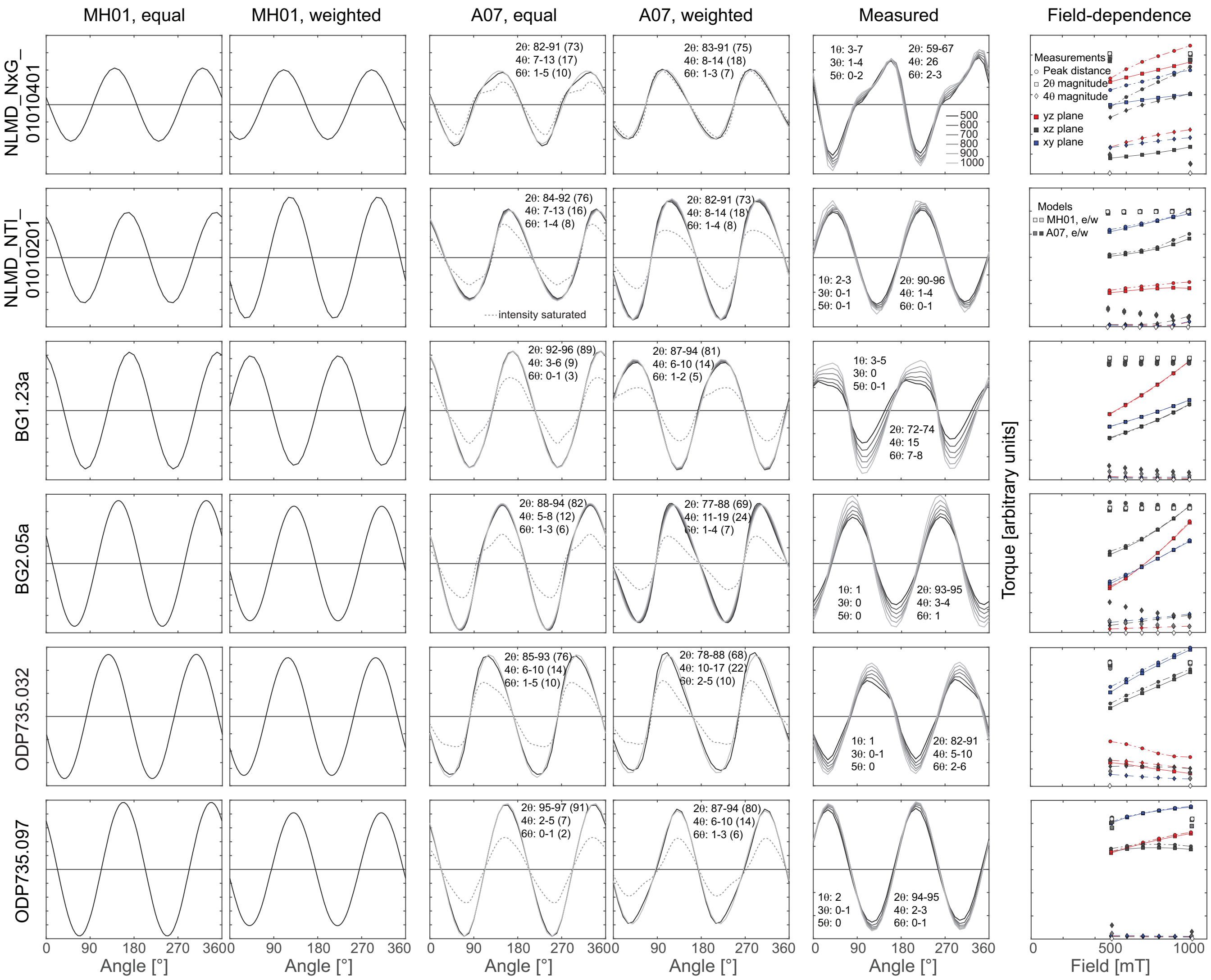

Figure 9. Modelled and measured torque curves for rock samples in different fields from 0.5 to 1 T. Models were calculated for only two fields for samples with >5000 particles to save computation time. Grey dotted line indicates the expected torque curve at the threshold field at which intensity saturates (∼300 mT), and after which the magnetization vector rotates towards the applied field direction to reach full saturation. Note that the vertical axis of this torque curve is shown to compare shape, but is not to scale with the other torque curves. Relative contributions of Fourier components are given for measurements, and those models that allow for components other than 2θ. For the latter, the range represents Fourier component proportions (in per cent) of the models calculated for 0.5–1 T, and the value in brackets represents Fourier contributions at the intensity saturation field. Field-dependence is shown as half peak-to-peak distance and magnitudes of 2θ and 4θ components for measurements and models. Note that a direct comparison is not possible, as the measurements also include paramagnetic contributions with a distinct linear dependence on the field squared, not considered in the models.

signal still changes (Figs 11 and 12). For small aspect ratios, and predominantly X or predominantly Z inclusions, the results of the MH01 and A07 models are comparable.

4 DISCUSSION

This study illustrates an example of magnetite shape anisotropy that can be represented by second-order tensors in low fields, but not in high fields, related to strong anisotropy, which occurs with elongated grains. In high fields, the magnetic anisotropy carried by clinopyroxene-hosted magnetite exsolutions contains up to *ca.* 30 per cent 4θ components in the [100]–[001] plane. Thus, the complex anisotropy appears to be an effect of high-field measurements, and is not a universal characteristic of pyroxene-hosted inclusions. Further investigations are needed to identify the threshold fields at which the magnetic anisotropy can no longer be adequately described by a second-order tensor. Such thresholds will help to estimate which anisotropy measurements are affected by non-linear behaviour. In general, second-order tensor anisotropies are expected as long as the relationship between field and magnetization is linear. This is typically true for low-field susceptibility and for anhysteretic remanence (ARM), as well as for most natural remanences (of thermal, detrital or chemical origin). However, some of the samples in this study show non-linear ARM acquisition behaviour even in low DC fields <0.2 mT. These samples may therefore possess non-linear anhysteretic remanence anisotropy, similar to samples with nonlinear thermoremanence acquisition (Selkin *et al.* 2007), and further work is needed to characterize their anisotropy.

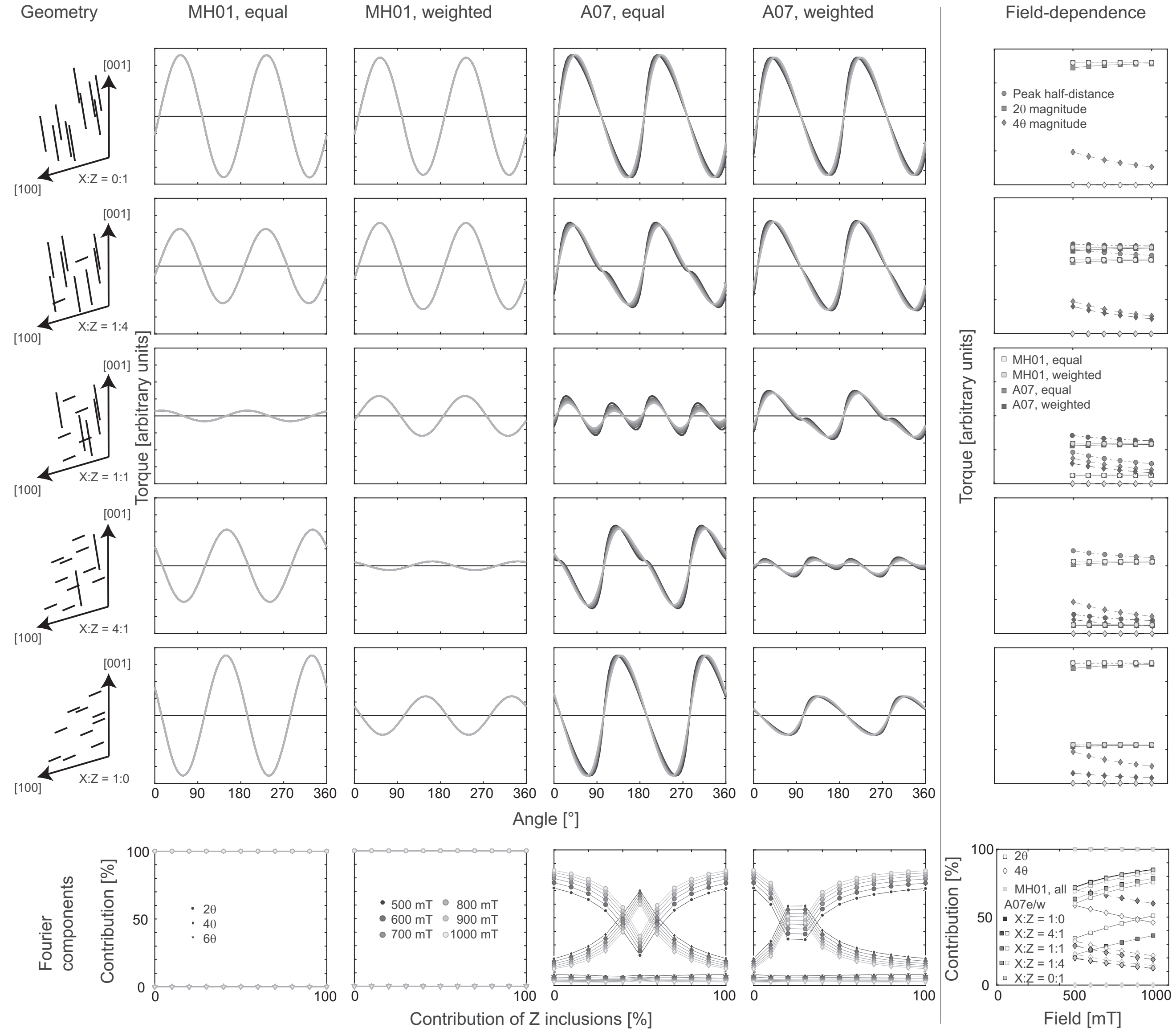

Figure 10. Expected torque curves, Fourier components, and field dependence for a single clinopyroxene crystal with various proportions of *X* and *Z* inclusions. All results shown for the [100]–[001] plane.

Many measurement and data processing schemes enforce the representation of magnetic fabrics using second-order tensors. If the rock anisotropy is more complex, this can have important consequences for structural and geodynamic interpretations, as well as for anisotropy corrections in palaeomagnetic studies, especially when magnetization is carried by clinopyroxene-hosted exsolutions. Similarly, while we have not measured the anisotropy of plagioclase-hosted inclusions in this study, with up to five sets of orientations it can be expected that also these are subject to complicated anisotropies. Conversely, these orientations are often multiplied by various feldspar twinning laws, which in turn yield orientation distributions that are closer to isotropic than those observed in pyroxene. We have also not investigated the anisotropy related to metallic particles hosted by olivine in chondritic meteorites, but given their specific orientation with respect to olivine and their expected high susceptibilities, their recorded remanence may be affected by similar complex anisotropies as observed here for pyroxene-hosted exsolved oxide inclusions. More work will be needed to define the high-field anisotropy of these samples. Furthermore, additional work is needed to quantify the effects of using overly simplistic second-order tensors on samples with more complex anisotropy. One such area of particular importance is the separation of paramagnetic and ferromagnetic components.

This study does not provide an alternative representation to the second-order tensor. However, it supports Coe (1966)'s statement that a less restrictive description of anisotropy will need to be developed, for some types of anisotropy measurements. We demonstrate how higher-order components can be described and quantified, and used as a complement to existing methods for representing complex anisotropy data (Flanders & Schuele 1964; Hrouda *et al.* 2018). Further, this study provides indications about the types of minerals and rock types that are likely to possess higher-order anisotropy components. In addition to clinopyroxenes with magnetite inclusions and clinopyroxene-bearing rocks, any other minerals containing oriented inclusions along several sets of crystallographic directions, for example plagioclase, amphibole, biotite and rocks

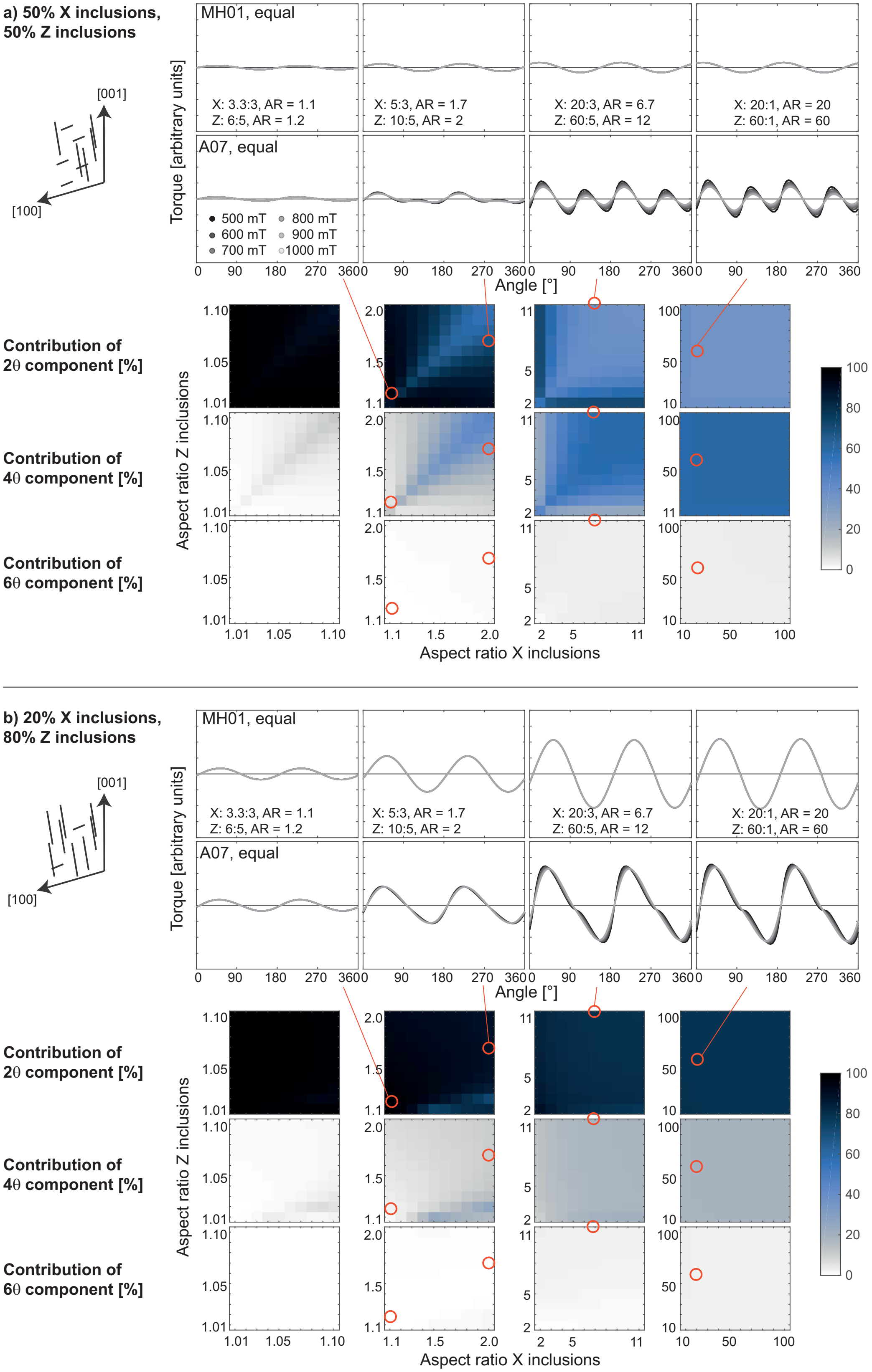

Figure 11. Examples of modelled torque curves in the [100]–[001] plane of a pyroxene with equal amounts of *X* and *Z* inclusions (a), and a pyroxene with 80 per cent Z inclusions and 20 per cent *X* inclusions (b). Numbers indicate the dimensions of *X* and *Z* exsolutions, as well as their aspect ratios (AR). In addition to torque curves for selected aspect ratios, the relative contributions of 2θ, 4θ and 6θ Fourier components are shown for a wide range of inclusion shapes. The colour scale indicates the percentage of each component. Red circles show the aspect ratios of the example torque curves. Torque curves are shown in arbitrary units, with the same vertical-axis range on all plots.

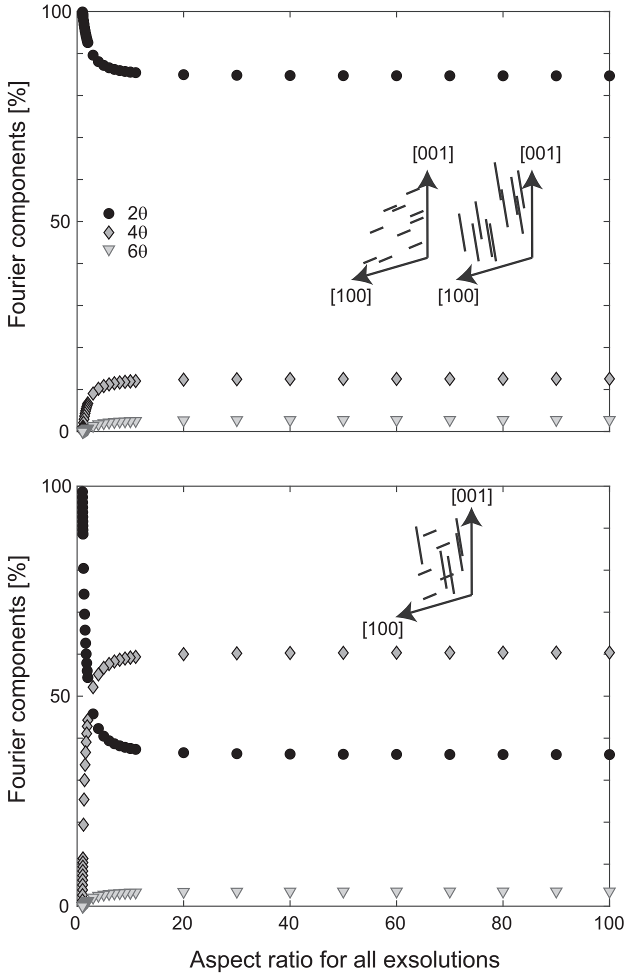

Figure 12. Fourier components of the torque signal as a function of aspect ratios for (top panel) either solely *X* inclusions or solely *Z* inclusions, or (bottom panel) equal amounts of *X* and *Z* inclusions. All inclusions are assumed to have the same aspect ratio.

containing these minerals, as well as dusty olivine in meteorites may display high-field anisotropies that cannot be described adequately by second-order tensors.

Many features in the measured torque data sets can be reproduced by the A07 model for torque in ellipsoidal soft magnetic materials with strong shape anisotropy. Note that certain characteristics of the torque signals observed in this study have been described in previous studies on different samples, where they were attributed to other sources. For example, 4*θ* components have been attributed to magnetite's magnetocrystalline anisotropy (Stacey 1960), 6*θ* components to the basal plane anisotropy in hematite and pyrrhotite (Flanders & Schuele 1964; Martin-Hernandez *et al.* 2008), and skewness as well as rotational hysteresis to non-saturated magnetization in hematite (Owens 1981). Keller & Schmidbauer (1996) observed rotational hysteresis in oxidized magnetite grains, and interpreted that it is related to stress at the maghemite-hematite interface. A different source was identified by Muxworthy (2002), who described rotational hysteresis in magnetite related to a high intrinsic anisotropy, which he attributed to metastable remanence. However, these observations were made in fields lower than those used in the present study. This variety of potential sources highlights the importance to carefully evaluate the origin of the measured anisotropy, preferably linking it to rock magnetic, chemical, and microstructural observations. Whereas rock magnetic methods are not sufficient to exclude the presence of hematite in samples dominated by magnetite, previous rock magnetic studies clearly indicated the presence of magnetite and Ti-magnetite in the samples investigated here (Worm 2001; Renne *et al.* 2002; Feinberg *et al.* 2004, 2005, 2006b; Finnes 2012; Biedermann *et al.* 2015, 2019a,b, 2020a,b). These results agree with chemical measurements that additionally identified sulphides in some samples. No hematite was identified in the chemical analyses, but if small volumes of oxidation rims surrounded the magnetite exsolutions, they would be below the resolution of the microprobe. In any case, abundant magnetite exsolutions (and some sulphides) were observed by both magnetic and chemical methods. The high aspect ratios displayed by the oxides in these samples increase their coercivity, and cause deviations of the magnetization vector from the field vector even at high fields, where magnetite is usually saturated. Similar to these observations, McElhinny & McFadden (1999, chapter 2) report that magnetite shape anisotropy results in high coercivity (300 mT compared to 60 mT expected for magnetocrystalline anisotropy), and Hrouda & Jelinek (1990) found that the torque signal of their magnetite-bearing samples was not saturated in their maximum field of 800 mT. While presence of hematite cannot be fully excluded in the rocks studied here, these observations, together with the good agreement between the measurements and A07 models, make us confident that strongly elongated or platy magnetite exsolutions within silicates are an alternative source for complex torque signals. The reason these exsolutions generate skewed torque signals or rotational hysteresis is similar to that described for hematite: the magnetization direction is not parallel to the applied field. In the case of hematite, the underlying cause is magnetocrystalline anisotropy, whereas in magnetite needles and platelets it is shape anisotropy. Despite their different origin, the observed characteristics are similar. The higher-order components of the anisotropy are then a consequence of the superposition of skewed signals of individual particles or groups of particles with similar aspect ratio and orientation.

Discrepancies between the details of the measured and modelled torque data can be explained by any of the following reasons: (1) The measurements are superpositions of para/diamagnetic, ferromagnetic, and antiferromagnetic subfabrics, whereas the models consider solely the shape anisotropy of magnetite, thus neglecting magnetite's magnetocrystalline anisotropy, distribution anisotropy, as well as contributions of minerals other than magnetite. (2) The image analysis was done on one surface, but the torque measurement includes the entire volume of the sample. Hence the agreement between model and measurement depends in part on the representativeness of the imaged surface. (3) The models contain some assumptions regarding the 3-D nature of the particles obtained from 2-D imaging. A full 3-D representation of these particles would result in different models, and represents a unique research opportunity for tomographic methods. (4) Some of the magnetite grains and inclusions are undoubtedly too small to be resolved in the BSE images. Thus, they contribute to the magnetic measurements, but are not included in the models. (5) Models were computed under the assumption that all oxides are magnetite, and that all oxides have the same saturation magnetization. Chemical analyses, however, suggest that ilmenite and sulphides are present in addition to magnetite, and that magnetite can have different Fe/Ti ratios. (6) Models assume that each imaged magnetite grain is homogeneous. However, microstructures related to intra-oxide exsolutions and cation ordering within magnetite may affect its magnetic properties considerably, for example increasing the grain's coercivity

(Putnis 1992; Harrison & Putnis 1997, chapter 12.6, Evans & Wayman 1974; Price 1980). (7) The single crystal models, especially those shown in Fig. 10, are simplified and idealized cases, assuming that all inclusions are perfectly aligned along two sets of orientations, and that all X, and all Z type inclusions have the same size and aspect ratio. Natural crystals, however, can be bent, kinked, have lattice defects, or even internal exsolution lamellae of their own, so that some dispersion is expected around these orientations. Additionally, there is a distribution of sizes and aspect ratios of inclusions in natural crystals.

The torque curves observed in single crystals and rock samples NLMD_NxG_01010401 and BG1.23a can be modelled based on the method described in Abbott *et al.* (2007), but not based on Martín-Hernández & Hirt (2001). The former set of equations is valid for magnetization that is saturated in intensity, but whose direction deviates from the applied field, whereas the latter requires full saturation. This indicates that the clinopyroxene-hosted magnetite inclusions in these samples have such high shape anisotropy, that their magnetization is not parallel to the field, that is they are not fully saturated. A result that supports this interpretation is that the importance of the 2θ contribution increases with increasing field for all single crystals in all three planes. This experimental observation is reflected in the models, and directly relates to expected field-dependent changes in magnetization direction. Similarly, the nonlinear increase of the 2θ magnitude and decrease of the 4θ magnitude with field, predicted by the A07 model and observed in single crystals from Tenerife, supports the conclusion that the magnetization vector deviates from the field direction, and that this deviation decreases with increasing field. The relative contribution of 2θ components does not always increase with field in rocks, which may be related to the presence of other phases with field-dependent magnetic properties, for example sulphides. Conversely, torque results measured for NLMD_NTl_01010201, BG2.05a and ODP735.097 are dominated by $2\ \theta$ components. Their inclusions may be less elongated, and therefore closer to saturation in both intensity and direction. The observed torque can be fitted better with a weighted model in BG1.23a, and with an unweighted model in most others. This may be explained by the magnetic anisotropy being dominantly carried by larger grains in the former, and smaller grains in the latter case. A related possible explanation is that specific size fractions of oxides differ in composition in terms of mineralogy or Ti substitution.

5 CONCLUSIONS

The shape and orientation of magnetite exsolutions in pyroxenes, and other silicates, is controlled by the crystal structure of the host silicate. Therefore, when pyroxenes are preferentially aligned in a rock, so will their oxide inclusions, resulting in magnetic anisotropy.

Unlike low-field anisotropy, the high-field magnetic anisotropy carried by magnetite exsolutions in clinopyroxene is complex, and cannot be adequately described by second-order tensors. We have shown that high-field torque curves measured on clinopyroxene single crystals, as well as clinopyroxene-bearing rocks display features that conflict with a second-order tensor representation: These include higher-order Fourier components (up to ∼30 per cent in the [100]–[001] plane of single crystals), skewness and asymmetry of torque curves. Additionally, the field-dependence of torque curves indicates that these magnetite exsolutions are not fully saturated, oppositely to what is assumed in fabric separation techniques.

The observed anisotropy, including the higher-order Fourier components, skewed and asymmetric torque curves, can be modelled using shape anisotropy, and particle size and orientation density as obtained from image analysis. Models have to be based on Abbott *et al.* (2007)'s torque equations, indicating that the oxide exsolutions in our samples are not fully saturated, most likely due to their high shape anisotropy. This shape anisotropy is also the reason why these exsolutions have high coercivities and are stable remanence carriers. A better understanding of the details of the magnetic anisotropy related to silicate-hosted exsolutions will lead to improved fabric separation, more reliable anisotropy corrections, and eventually make these exsolutions even more useful in palaeomagnetic studies on ancient rocks or extraterrestrial materials.

ACKNOWLEDGEMENTS

Anette von der Handt is thanked for valuable help with the microprobe and imaging. Eric Ferré, Fatima Martin-Hernandez and an anonymous reviewer as well as editor Eduard Petrovsky are gratefully acknowledged for their detailed and critical evaluation of the manuscript. This study was funded by the Swiss National Science Foundation, projects 167608/167609 and 176917.

REFERENCES

Abbott, J.J., Ergeneman, O., Kummer, M.P., Hirt, A.M. & Nelson, B.J., 2007. Modeling magnetic torque and force for controlled manipulation of soft-magnetic bodies, *IEEE Trans. Rob.,* **23,** 1247–1252.

Aitken, M.J., Alcock, P.A., Bussell, G.D. & Shaw, C.J., 1981. Archaeomagnetic determination of the past geomagnetic intensity using ancient ceramics: allowance for anisotropy, *Archaeomatry,* **23,** 53–64.

Anson, G.L. & Kodama, K.P., 1987. Compaction-induced inclination shallowing of the post-depositional remanent magnetization in a synthetic sediment, *Geophys. J. R. astr. Soc.,* **88,** 673–692.

Bergmüller, F., Bärlocher, C., Geyer, B., Grieder, M., Heller, F. & Zweifel, P., 1994. A torque magnetometer for measurements of the high-field anisotropy of rocks and crystals, *Meas. Sci. Technol.,* **5,** 1466–1470.

Biedermann, A.R., Bilardello, D., Jackson, M., Tauxe, L. & Feinberg, J.M., 2019a. Grain-size-dependent remanence anisotropy and its implications for paleodirections and paleointensities - proposing a new approach to anisotropy corrections, *Earth planet. Sci. Lett.,* **512,** 111–123.

Biedermann, A.R., Jackson, M., Bilardello, D. & Feinberg, J.M., 2019b. Anisotropy of (partial) isothermal remanent magnetization: DC-field-dependence and additivity, *Geophys. J. Int.,* **218,** 1428–1441.

Biedermann, A.R., Jackson, M., Bilardello, D. & Feinberg, J.M., 2020a. Anisotropy of full and partial anhysteretic remanence across different rock types: 2. Coercivity-dependence of remanence anisotropy, *Tectonics,* **39,** doi:10.1029/2018TC005285.

Biedermann, A.R., Jackson, M., Stillinger, M.D., Bilardello, D. & Feinberg, J.M., 2020b. Anisotropy of full and partial anhysteretic remanence across different rock types: 1. Are partial anhysteretic remanence anisotropy tensors additive? *Tectonics,* **39,** doi:10.1029/2018TC005284.

Biedermann, A.R., Pettke, T., Bender Koch, C. & Hirt, A.M., 2015. Magnetic anisotropy in clinopyroxene and orthopyroxene single crystals, *J. geophys. Res.,* **120,** 1431–1451.

Bilardello, D. & Kodama, K.P., 2010. A new inclination shallowing correction of the Mauch Chunk Formation of Pennsylvania, based on high-field AIR results: implications for the Carboniferous North American APW path and Pangea reconstructions, *Earth planet. Sci. Lett.,* **299,** 218–227.

Bogue, S.W., Gromme, S. & Hillhouse, J.W., 1995. Paleomagnetism, magnetic anisotropy, and mid-Cretaceous paleolatitude of the Duke Island (Alaska) ultramafic complex, *Tectonics,* **14,** 1133–1152.

Borradaile, G.J. & Henry, B., 1997. Tectonic applications of magnetic susceptibility and its anisotropy, *Earth Sci. Rev.,* **42,** 49–93.

Borradaile, G.J. & Jackson, M., 2010. Structural geology, petrofabrics and magnetic fabrics (AMS, AARM, AIRM), *J. Struct. Geol.,* **32,** 1519–1551.

Bown, M.G. & Gay, P., 1959. The identification of oriented inclusions in pyroxene crystals, *Am. Mineral.,* **44,** 592–602.

Coe, R.S., 1966. Analysis of magnetic shape anisotropy using second-rank tensors, *J. geophys. Res.,* **71,** 2637–2644.

Cottrell, R.D. & Tarduno, J.A., 1999. Geomagnetic paleointensity derived from single plagioclase crystals, *Earth planet. Sci. Lett.,* **169,** 1–5.

Davis, K.E., 1981. Magnetite rods in plagioclase as the primary carrier of stable NRM in ocean floor gabbros, *Earth planet. Sci. Lett.,* **55,** 190–198.

Doukhan, N., Ingrin, J., Doukhan, J.C. & Latrous, K., 1990. Coprecipitation of magnetite and amphibole in black star diopside: a TEM study, *Am. Mineral.,* **75,** 840–846.

Einsle, J.F. *et al.*, 2016. Multi-scale three-dimensional characterization of iron particles in dusty olivine: implications for paleomagnetism of chondritic meteorites, *Am. Mineral.,* **101,** 2070–2084.

Evans, M.E., McElhinny, M.W. & Gifford, A.C., 1968. Single domain magnetite and high coercivities in a gabbroic intrusion, *Earth planet. Sci. Lett.,* **4,** 142–146.

Evans, M.E. & Wayman, M.L., 1974. An investigation of the role of ultrafine titanomagnetite intergrowths in paleomagnetism, *Geophys. J. R. astr. Soc.,* **36,** 1–10.

Feinberg, J.M., Harrison, R.J., Kasama, T., Dunin-Borkowski, R.E., Scott, G.R. & Renne, P.R., 2006a. Effects of internal mineral structures on the magnetic remanence of silicate-hosted titanomagnetite inclusions: an electron holography study, *J. geophys. Res.,* **111,** doi:10.1029/2006JB004498.

Feinberg, J.M., Scott, G.R., Renne, P.R. & Wenk, H.-R., 2005. Exsolved magnetite inclusions in silicates: features determining their remanence behavior, *Geology,* **33,** 513.

Feinberg, J.M., Wenk, H.-R., Renne, P.R. & Scott, G.R., 2004. Epitaxial relationships of clinopyroxene-hosted magnetite determined using electron backscatter diffraction (EBSD) technique, *Am. Mineral.,* **89,** 462–466.

Feinberg, J.M., Wenk, H.-R., Scott, G.R. & Renne, P.R., 2006b. Preferred orientation and anisotropy of seismic and magnetic properties in gabbronorites from the Bushveld layered intrusion, *Tectonophysics,* **420,** 345–356.

Finnes, E.M., 2012, A rock and paleomagnetic characterization of the Duluth Complex layered series intrusions associated with the Nokomis Deposit in NE Minnesota, *MSc thesis*, University of Minnesota, Minneapolis, USA.

Flanders, P.J. & Remeika, J.P., 1965. Magnetic properties of hematite single crystals, *Philos. Mag.,* **11,** 1271–1288.

Flanders, P.J. & Schuele, W.J., 1964. Anisotropy in the basal plane of hematite single crystals, *Philos. Mag.,* **9,** 485–490.

Fleet, M.E., Bilcox, G.A. & Barnett, R.L., 1980. Oriented magnetite inclusions in pyroxenes from the Grenville Province, *Can. Mineral.,* **18,** 89–99.

Fuller, M.D., 1960. Anisotropy of susceptibility and the natural remanent magnetization of some Welsh slates, *Nature,* **186,** 790–792.

Fuller, M.D., 1963. Magnetic anisotropy and paleomagnetism, *J. geophys. Res.,* **68,** 293–309.

Geissman, J.W., Harlan, S.S. & Brearley, A.J., 1988. The physical isolation and identification of carriers of geologically stable remanent magnetization: paleomagnetic and rock magnetic microanalysis and electron microscopy, *Geophys. Res. Lett.,* **15,** 479–482.

Girdler, R.W., 1961. The measurement and computation of anisotropy of magnetic susceptibility of rocks, *Geophys. J. R. astr. Soc.,* **5,** 34–44.

Grégoire, V., Darrozes, P., Gaillot, P. & Nédélec, A., 1998. Magnetite grain shape fabric and distribution anisotropy vs rock magnetic fabric: a three-dimensional case study, *J. Struct. Geol.,* **20,** 937–944.

Grégoire, V., De Saint-Blanquat, M., Nédélec, A. & Bouchez, J.-L., 1995. Shape anisotropy versus magnetic interactions of magnetite grains: experiments and application to AMS in granitic rocks, *Geophys. Res. Lett.,* **22,** 2765–2768.

Hargraves, R.B., 1959. Magnetic anisotropy and remanent magnetism in hemo-ilmenite from ore deposits at Allard Lake, Quebec, *J. geophys. Res.,* **64,** 1565–1578.

Hargraves, R.B. & Young, W.M., 1969. Source of stable remanent magnetism in Lambertville diabase, *Am. J. Sci.,* **267,** 1161–1177.

Harrison, R.J. & Putnis, A., 1997. Interaction between exsolution microstructures and magnetic properties of the magnetite-spinel solid solution, *Am. Mineral.,* **82,** 131–142.

Hrouda, F., Chadima, M. & Jezek, J., 2018. Anisotropy of susceptibility in rocks which are magnetically nonlinear even in low fields, *Geophys. J. Int.,* **213,** 1792–1803.

Hrouda, F. & Jelinek, V., 1990. Resolution of ferrimagnetic and paramagnetic anisotropies in rocks, using combined low-field and high-field measurements, *Geophys. J. Int.,* **103,** 75–84.

Jackson, M.J., Banerjee, S.K., Marvin, J.A., Lu, R. & Gruber, W., 1991. Detrital remanence, inclination errors, and anhysteretic remanence anisotropy: quantitative model and experimental results, *Geophys. J. Int.,* **104,** 95–103.

Jelinek, V., 1977. *The Statistical Theory of Measuring Anisotropy of Magnetic Susceptibility of Rocks and its Application,* Geofyzika.

Keller, R. & Schmidbauer, E., 1996. Magnetic properties and rotational hysteresis losses of oxidized ∼250 nm Fe3O4 particles, *Journal of Magnetism and Magnetic Materials,* **162,** 85–90.

King, R.F., 1955. The remanent magnetism of artificially deposited sediments, *Geophys. Suppl. Mon. Not. R. astr. Soc.,* **7,** 115–134.

Kodama, K.P., 2012. *Paleomagnetism of Sedimentary Rocks: Process and Interpretation,* Wiley-Blackwell.

Lagroix, F. & Borradaile, G.J., 2000. Magnetic fabric interpretation complicated by inclusions in mafic silicates, *Tectonophysics,* **325,** 207–225.

Lappe, S.-C. *et al.*, 2011. Mineral magnetism of dusty olivine: a credible recorder of pre-accretionary remanence, *Geochem. Geophys. Geosyst.,* **12,** doi:10.1029/2011GC003811.

Leroux, H., Libourel, G., Lemelle, L. & Guyot, F., 2003. Experimental study and TEM characterization of dusty olivines in chondrites: evidence for formation by in situ reduction, *Meteorit. Planet. Sci.,* **38,** 81–94.

Lowrie, W., Hirt, A.M. & Kligfield, R., 1986. Effects of tectonic deformation on the remanent magnetization of rocks, *Tectonics,* **5,** 713–722.

Martin-Hernandez, F., Bominaar-Silkens, I.M., Dekkers, M.J. & Kees Maan, J., 2006. High-field cantilever magnetometry as a tool for the determination of the magnetocrystalline anisotropy of single crystals, *Tectonophysics,* **418,** 21–30.

Martin-Hernandez, F., Dekkers, M.J., Bominaar-Silkens, I.M.A. & Maan, J.C., 2008. Magnetic anisotropy behaviour of pyrrhotite as determined by low- and high-field experiments, *Geophys. J. Int.,* **174,** 42–54.

Martin-Hernandez, F. & Guerrero-Suarez, S., 2012. Magnetic anisotropy of hematite natural crystals: high field experiments, *Int. J. Earth Sci.,* **101,** 637–647.

Martín-Hernández, F. & Hirt, A.M., 2001. Separation of ferrimagnetic and paramagnetic anisotropies using a high-field torsion magnetometer, *Tectonophysics,* **337,** 209–221.

McElhinny, M.W. & McFadden, P.L., 1999. *Paleomagnetism: Continents and Oceans,* Academic Press.

Morgan, G.E. & Smith, P.P.K., 1981. Transmission electron microscope and rock magnetic investigations of remanence carriers in a Precambrian metadolerite, *Earth planet. Sci. Lett.,* **53,** 226–240.

Murthy, G.S., Evans, M.E. & Gough, D.I., 1971. Evidence of single-domain magnetite in the Michikamau anorthosite, *Can. J. Earth Sci.,* **8,** 361–370.

Muxworthy, A.R., 2002. Magnetic hysteresis and rotational hysteresis properties of hydrothermally grown multidomain magnetite, *Geophys. J. Int.,* **149,** 805–814.

Nye, J.F., 1957. *Physical Properties of Crystals: Their Representation by Tensors and Matrices,* Clarendon Press.

Osborn, J.A., 1945. Demagnetizing factors of the general ellipsoid, *Phys. Rev.,* **67,** 351–357.

Owens, W.H., 1981. A simple model for non-vanishing rotational hysteresis in haematite, *Phys. Earth planet. Inter.,* **27,** 106–113.

Palmer, H.C. & Carmichael, C.M., 1973. Paleomagnetism of some Grenville Province Rocks, *Can. J. Earth Sci.,* **10,** 1175–1190.

Price, G.D., 1980. Exsolution microstructures in titanomagnetites and their magnetic significance, *Phys. Earth planet. Inter.,* **23,** 2–12.

Putnis, A., 1979. Electron petrography of high-temperature oxidation in olivine from the Rhum Layered Intrusion, *Mineral. Mag.,* **43,** 293–296.

Putnis, A., 1992. *Introduction to Mineral Sciences,* Cambridge Univ. Press.

Renne, P.R., Scott, G.R., Glen, J.M.G. & Feinberg, J.M., 2002. Oriented inclusions of magnetite in clinopyroxene: Source of stable remanent magnetization in gabbros of the Messum Complex, Namibia, *Geochem. Geophys. Geosyst.,* **3,** 1079.

Rogers, J., Fox, J.M.W. & Aitken, M.J., 1979. Magnetic anisotropy in ancient pottery, *Nature,* **277,** 644–646.

Schindelin, J. *et al.*, 2012. Fiji: an open-source platform for biological image analysis, *Nat. Methods,* **9,** 676–682.

Schlinger, C.M. & Veblen, D.R., 1989. Magnetism and transmission electron microscopy of Fe-Ti oxides and pyroxenes in a granulite from Lofoten, Norway, *J. geophys. Res.,* **94,** 14009–14026.

Schneider, C.A., Rasband, W.S. & Eliceiri, K.W., 2012. NIH image to ImageJ: 25 years of image analysis, *Nat. Methods,* **9,** 671–675.

Scofield, N. & Roggenthen, W.M., 1986. Petrologic evolution of plagioclase-rich cumulates from the Wichita Mountains, oklahoma: effects upon magnetic remanence properties, *Geology,* **14,** 908–911.

Selkin, P.A., Gee, J.S., Meurer, W.P. & Hemming, S.R., 2008. Paleointensity record from the 2.7 Ga Stillwater Complex, Montana, *Geochem. Geophys. Geosyst.,* **9,** Q12023, doi:10.1029/2008GC001950.

Selkin, P.A., Gee, J.S. & Tauxe, L., 2007. Nonlinear thermoremanence acquisition and implications for paleointensity data, *Earth planet. Sci. Lett.,* **256,** 81–89.

Selkin, P.A., Gee, J.S., Tauxe, L., Meurer, W.P. & Newell, A.J., 2000. The effect of remanence anisotropy on paleointensity estimates: a case study from the Archean Stillwater Complex, *Earth planet. Sci. Lett.,* **183,** 403–416.

Sobolev, P.O., 1990. Orientation of acicular iron-ore mineral inclusions in plagioclase, *Int. Geol. Rev.,* **32,** 616–628.

Stacey, F.D., 1960. Magnetic anisotropy of igneous rocks, *J. geophys. Res.,* **65,** 2429–2442.

Stamatakos, J. & Kodama, K.P., 1991. Flexural flow folding and the paleomagnetic fold test: an example of strain reorientation of remanence in the Mauch Chunk Formation, *Tectonics,* **10,** 807–819.

Syono, Y., 1965. Magnetocrystalline anisotropy and magnetostriction of Fe_3O_4–Fe_2TiO_4 series, with special application to rock magnetism, *Jpn. J. Geophys.,* **4,** 71–143.

Tarduno, J.A., Cottrell, R.D. & Smirnov, A.V., 2006. The paleomagnetism of single silicate crystals: recording geomagnetic field strength during mixed polarity intervals, superchrons, and inner core growth, *Rev. Geophys.,* **44,** doi:10.1029/2005RG000189.

Tauxe, L. & Kent, D.V., 2004. A simplified statistical model for the geomagnetic field and the detection of shallow bias in paleomagnetic inclinations: was the ancient magnetic field dipolar? *Geophys. Monogr. Ser.,* **145,** doi:10.1029/145GM08

Tauxe, L., Kodama, K.P. & Kent, D.V., 2008. Testing corrections for paleomagnetic inclination error in sedimentary rocks: a comparative approach, *Phys. Earth planet. Inter.,* **169,** 152–165.

Wenk, H.-R., Chen, K. & Smith, R., 2011. Morphology and microstructure of magnetite and ilmenite inclusions in plagioclase from Adirondack anorthositic gneiss, *Am. Mineral.,* **96,** 1316–1324.

Worm, H.-U., 2001. Magnetic stability of oceanic gabbros from ODP Hole 735B, *Earth planet. Sci. Lett.,* **193,** 287–302.

Wu, Y.T., Fuller, M. & Schmidt, V.A., 1974. Microanalysis of NRM in a granodiorite intrusion, *Earth planet. Sci. Lett.,* **23,** 275–285.

Xu, W., Geissman, J.W., Van der Voo, R. & Peacor, D.R., 1997. Electron microscopy of iron oxides and implications for the origin of magnetizations and rock magnetic properties of banded series rocks of the stillwater complex, Montana, *J. geophys. Res.,* **102,** 12 139–12 157.

Yu, Y. & Dunlop, D.J., 2001. Paleointensity determination on the Late Precambrian Tudor Gabbro, Ontario, *J. geophys. Res.,* **106,** 26 331–26 343.